Science
AAAS

Supplementary Materials for

Mechanism-based design of agents that selectively target drug-resistant glioma

Kingson Lin *et al*.

Corresponding authors: Ranjit S. Bindra, ranjit.bindra@yale.edu; Seth B. Herzon, seth.herzon@yale.edu

Science **377**, 502 (2022)
DOI: 10.1126/science.abn7570

The PDF file includes:

Other Supplementary Material for this manuscript includes the following:

Materials and Methods

General Chemical Experimental Procedures

All reactions were performed in single-neck, flame dried round-bottom flasks fitted with rubber septa under a positive pressure of argon, unless otherwise specified. Air- and moisture-sensitive liquids were transferred via syringe or stainless-steel cannula. Organic solutions were concentrated by rotary evaporation at 31 °C, unless otherwise noted. Flash-column chromatography was performed as described by Still et al. (*54*), employing silica gel (SiliaFlash® P60, 60 Å, 40-63 μm particle size) purchased from Silicycle (Québec, Canada). Analytical thin-layered chromatography (TLC) was performed using glass plates pre-coated with silica gel (250 μm, 60 Å pore size) embedded with a fluorescent indicator (254 nm). TLC plates were visualized by exposure to ultraviolet (UV) light.

Chemical Methods

Commercial solvents, chemicals, and reagents were used as received with the follow exceptions. Dichloromethane, tetrahydrofuran, and toluene were purified according to the method of Pangborn et al (*55*). Triethylamine was distilled from calcium hydride under an atmosphere of nitrogen immediately prior to use. *N*,*N*-Di-*iso*-propylethylamine was distilled from calcium hydride under argon immediately prior to use. The diazonium **S7** (*56*), the imidazolyl triazene **1b** (*57*), the imidazolyl triazene **4b** (*58*), the imidazolyl triazene **9** (*59*), the imidazolyl triazene **12b** (*60*), and the imidazolyl triazene **13** (*57*) were synthesized according to published procedures.

Chemistry Instrumentation

Proton nuclear magnetic resonance (^{1}H NMR) were recorded at 400 or 600 megahertz (MHz) at 23 °C, unless otherwise noted. Chemical shifts are expressed in parts per million (ppm, δ scale) downfield from tetramethylsilane and are referenced to residual proton in the NMR solvent ($(CD_3)SO(CHD_2)$, δ 2.50). Data are represented as follows: chemical shift, multiplicity (s = singlet, d = doublet, t = triplet, q = quartet, m = multiplet and/or multiple resonances, b = broad, app = apparent), coupling constant in Hertz (Hz), integration, and assignment. Proton-decoupled carbon nuclear magnetic resonance spectra (^{13}C NMR) were recorded at 150 MHz at 23 °C, unless otherwise noted. Chemical shifts are expressed in parts per million (ppm, δ scale) downfield from tetramethylsilane and are referenced to the carbon resonances of the solvent (DMSO-d_6, δ 39.52). ^{1}H-^{1}H gradient-selected correlation spectroscopy (COSY), ^{1}H-^{13}C heteronuclear single quantum coherence (HSQC), and ^{1}H-^{13}C gradient-selected heteronuclear multiple bond correlation (gHMBC) were recorded at 600 MHz at 23 °C, unless otherwise noted. Carbon-decoupled fluorine nuclear magnetic resonance spectra (^{19}F NMR) were recorded at 396 MHz at 23 °C, unless otherwise noted. Chemical shifts are expressed in parts per million (ppm, δ scale) downfield from tetramethylsilane. Attenuated total reflectance Fourier transform infrared (ATR-FTIR) spectra were obtained using a Thermo Electron Corporation Nicolet 6700 FTIR spectrometer referenced to a polystyrene standard. Data are represented as follows: frequency of absorption (cm^{-1}), intensity of absorption (s = strong, m = medium, w = weak, br = broad). Analytical liquid chromatography-mass spectroscopy (LCMS) was performed on a Waters instrument equipped with a reverse-phase C_{18} column (1.7 μm particle size, 2.1 × 50 mm). Samples were eluted with a linear gradient of 5% acetonitrile–water containing 0.1% formic acid→100% acetonitrile containing 0.1% formic acid over 0.75 min, followed by 100% acetonitrile containing 0.1% formic acid for 0.75 min, at a flow rate of 800 μL/min. HRMS were obtained on a Waters UPLC/HRMS

instrument equipped with a dual API/ESI high resolution mass spectrometry detector and photodiode array detector.

Biological Materials

Temozolomide (TMZ, **1a**), lomustine (**14**), O^6-benzylguanine (O^6BG), doxorubicin, and olaparib were purchased from Selleck Chemicals. Methyl methanesulfonate (MMS) was purchased from Alfa-Aesar. Mitozolomide (MTZ, **12a**) was purchased from Enamine. Mitomycin C (MMC), *N*-ethylmaleimide (NEM), *N*-acetyl-L-cysteine (NAC), and cisplatin were purchased from Sigma. TMZ (**1a**, 100 mM stock), O^6BG (100 mM stock), MTZ (**12a**, 100 mM stock), MMS (500 mM stock) and NAC (100 mM stock) were dissolved in DMSO and stored at –80 ºC. MMC (10 mM stock), lomustine (**14**, 100 mM stock), doxorubicin (10 mM stock), and olaparib (18.3 mM stock) were dissolved in DMSO and stored at –20 ºC. NEM (400 mM stock) was dissolved in EtOH and stored at –20 ºC. Cisplatin (5 mM stock) was dissolved in H_2O and stored at 4 ºC for up to 7 days.

Cell Culture

LN229 MGMT– and MGMT+ cell lines were a gift from B. Kaina (Johannes Gutenberg University Mainz, Mainz, Germany) and grown in DMEM with 10% FBS (Gibco). DLD1 BRCA2+/– and BRCA2–/– cell lines (Horizon Discovery, Cambridge, UK) were grown in RPMI 1640 with 10% FBS. HCT116 MLH1–/– and HCT116+Chr3 cell lines (*61*) were a gift from T. Kunkel (National Institute of Environmental Health Sciences, Durham, NC) and grown in DMEM with 10% FBS, with 0.5 µg/mL G418 (Sigma) for HCT116+Chr3 cells. PD20 cell lines complemented with empty vector (+EV), wildtype FANCD2 (+FD2), or K561R ubiquitination-mutant FANCD2 (+KR) were a gift from G. Kupfer and P. Glazer (Yale University, New Haven, CT) and grown in DMEM with 10% FBS. PEO1 and PEO4 cell lines (*62*) were a gift from T. Taniguchi (Fred Hutchinson Cancer Research Center, Seattle, WA) and were grown in DMEM with 10% FBS. BJ fibroblasts (normal human fibroblast cells) were purchased from ATCC (CRL-2522) and grown in DMEM with 10% FBS. NER isogenic MEFs were a gift from F. Rogers (Yale University, New Haven, CT) and were grown in DMEM with 10% FBS. All human cell lines were validated by short tandem repeat profiling (excluding BJ fibroblasts which were used within 6 passages of receiving from ATCC) and confirmed negative for mycoplasma by quantitative RT-PCR.

MMR Protein shRNA Knockdown

pGIPZ lentiviral shRNA vectors targeting MSH2, MSH6, MLH1, PMS2, and MSH3 were purchased from Horizon Discovery as detailed below. Lentiviral particles were produced in HEK293T cells via co-transfection with lentiviral shRNA plasmid, pCMV-VSV-G envelope plasmid (Addgene, #8454) and psPAX2 packaging plasmid (Addgene, #12260), using Lipofectamine 3000 Reagent (Invitrogen, L3000001) per manufacturer's protocol. Viral particles were harvested 48 h post-transfection and used to transduce LN229 MGMT+/– cells in the presence of 8 µg/mL polybrene. Selection of pooled cells with lentiviral expression was established with 1 µg/mL puromycin 48 h post-transduction for 3 to 4 days. Single cell cloning was performed by limiting dilution and protein knockdown was confirmed by western blotting.

Protein Target	pGIPZ Human Lentiviral shRNA Clone	Mature Antisense Sequence
MSH2	RHS4430-200305416	TTACTAAGCACAACACTCT
MSH6	RHS4430-200281418	TACACATTACTTTGAATCC
MLH1	RHS4430-200268977	AACTGAGAAACTAATGCCT
PMS2	RHS4430-200253216	TTCACAGCTACATCAACCT
MSH3	RHS4430-200158125	TTTCTTGCAAATGCATTCG

Western Blotting

For phospho-protein analysis experiments, cells were lysed in 1X RIPA buffer (Cell Signaling Technology, #9806) supplemented with 1X Protease Inhibitor Cocktail (Roche) and 1X PhosSTOP Phosphatase Inhibitor Cocktail (Sigma). For all other western blot analyses, cells were lysed in lysis buffer (50 mM HEPES, 250 mM NaCl, 5 mM EDTA, 1% NP-40) supplemented with 1X Protease Inhibitor Cocktail (Roche). The de-ubiquitination inhibitor *N*-ethylmaleimide (NEM, 4 mM) was added in FANCD2 ubiquitination analysis experiments. Proteins were separated using NuPAGE 4–12% Bis-Tris or 3–8% Tris-Acetate Gels (Invitrogen) and transferred to Immobilon-P PVDF membrane (Millipore) for western blotting. Membranes were blocked with 5% milk in TBS-T for 1 h prior to primary antibody addition overnight at 4 °C. Primary antibodies were used under the following conditions: mouse anti-CHK1 (Cell Signaling Technology, #2360), 1/1000 in 5% milk; rabbit anti-CHK2 (Cell Signaling Technology, #6334), 1/1000 in 5% BSA; rabbit anti-FANCD2 (Cell Signaling Technology, #16323), 1/1000 in 5% BSA; HRP-conjugated anti-GAPDH (ProteinTech HRP-60004), 1/10,000 in 5% milk; rabbit anti-MGMT (Cell Signaling Technology, #2739), 1/1000 in 5% BSA; rabbit anti-MLH1 (Cell Signaling Technology, #4256), 1/1000 in 5% BSA; mouse anti-MSH2 (Cell Signaling Technology, #2850), 1/1000 in 5% milk; mouse anti-MSH3 (BD Biosciences, BD611390), 1/500 in 5% milk; mouse anti-MSH6 (BD Biosciences, BD610918), 1/1000 in 5% milk; rabbit anti-phospho-CHK1 (S345) (Cell Signaling Technology, #2341), 1/1000 in 5% BSA; rabbit anti-phospho-CHK2 (T68) (Cell Signaling Technology, #2661), 1/1000 in % BSA; mouse anti-PMS2 (Santa Cruz, sc-25315), 1/100 in 5% milk; mouse anti-Vinculin (Santa Cruz, sc-25336), 1/1000 in 5% milk. Anti-mouse IgG HRP-conjugated antibody (Cell Signaling Technology, #7076) and anti-rabbit IgG HRP-conjugated antibody (Cell Signaling Technology, #93702) were added at 1/5000 in 5% milk for 1 h. Chemiluminescence detection was performed with Clarity Max Western ECL Substrate (Bio-Rad) and blots were imaged on a ChemiDoc XRS+ Molecular Imager (Bio-Rad). Where shown, bands were quantified using ImageJ software.

Short-term Cell Viability Assay

Cells were seeded in 96-well plates at 1000 or 2000 cells/well and allowed to adhere at 23 ºC for 60 min and then incubated overnight at 37 °C. Cells were treated with indicated concentrations of compounds in triplicate for 4-6 days prior to fixation with 3.7% paraformaldehyde and nuclear staining with 1 µg/mL Hoechst 33342 dye. Cells were imaged on a Cytation 3 imaging reader (BioTek) and quantified using CellProfiler software (*63*).

Clonogenic Cell Survival Assay

Cells were trypsinized, washed, counted, and diluted in a medium containing various concentrations of drug. They were then immediately seeded in six-well plates in triplicate at three-fold dilutions, ranging from 9000 to 37 cells per well. Depending on colony size, these plates were

kept in the incubator for 10 to 14 days. After incubation, colonies were washed in phosphate-buffered saline (PBS), stained with crystal violet, counted, and quantified.

IR Alkaline Comet Assay

Assay was performed utilizing the CometAssay Kit (Trevigen) according to the alkaline assay protocol, with the addition of slide irradiation post-lysis (*64*). Cells were trypsinized, washed with 1X PBS, added to melted Comet LMAgarose (Trevigen), and spread on Trevigen CometSlides at a density of 1000 cells per sample in 50 µL. Lysis solution (Trevigen) with 10% DMSO was added overnight at 4 ºC. Slides were removed from lysis buffer and irradiated to 0 or 10 Gy using an XRAD 320 X-Ray System (Precision X-Ray) at 320 kV, 12.5 mA, and 50.0 cm SSD, with a 2 mm Al filter and 20 cm × 20 cm collimator. Slides were then placed in alkaline buffer (200 mM NaOH, 1 mM EDTA) for 45 min, followed by electrophoresis in 850 mL alkaline buffer for 45 min at 4 ºC. Slides were washed and stained with SYBR gold (Invitrogen) per Trevigen assay protocol. Slides were imaged on a Cytation 3 imaging reader (BioTek), and comets were analyzed using CometScore 2.0 software (TriTek).

Genomic DNA Denaturing Gel Electrophoresis

Assay was adapted from (*33*). Cells were trypsinized, washed with 1X PBS, and stored at –80 ºC prior to processing. Genomic DNA was extracted with the DNeasy Blood & Tissue Kit (Qiagen) per kit protocol. A 0.7% agarose gel was prepared in 100 mM NaCl-2mM EDTA (pH 8) and soaked in 40 mM NaOH–1 mM EDTA running buffer for 2 h. Genomic DNA (400 ng/well) was then loaded in 1X BlueJuice loading buffer (Invitrogen) and subjected to electrophoresis at 2 V/cm for 30 min, followed by 3 V/cm for 2 h. The gel was neutralized in 150 mM NaCl–100 mM Tris (pH 7.4) for 30 min, twice, and then stained with 1X SYBR Gold in 150 mM NaCl–100 mM Tris (pH 7.4) for 90 min. Imaging was performed on a ChemiDoc XRS+ Molecular Imager (Bio-Rad).

Plasmid Linearization Assay

To set up the linearization reactions, 20 units of EcoRI-HF (New England Biolabs) was mixed with 20 µg 2686 bp pUC19 vector DNA in CutSmart buffer (New England Biolabs), pH 7.9, in a total volume of 1000 µL for 30 min at 37 °C. The CutSmart buffer contains 50 mM potassium acetate, 20 mM Tris acetate, 10 mM magnesium acetate, and 100 µg/mL BSA. The reacted DNA was then purified using PCR cleanup kit and quantified using the NanoDrop One (Thermo Fisher). The DNA was then stored at −20 °C before use in *in vitro* DNA cross-linking assays or melting temperature analysis.

In Vitro DNA Cross-linking Assays

Linearized pUC19 DNA, prepared as described above, was used for *in vitro* DNA cross-linking assays. For each condition, 200 ng of linearized pUC19 DNA (15.4 µM base pairs) was incubated with the indicated concentration of drug in 20 µL. Drug stock concentrations were made in DMSO such that each reaction contained a fixed 5% DMSO concentration. Reactions were conducted in 100 mM Tris buffer (pH 7.4). Cisplatin (Sigma) and DMSO vehicle were used as positive and negative controls, respectively. Reactions were conducted for 6–36 h at 37 °C. The DNA was stored at −80 °C until electrophoretic analysis. For gel electrophoresis, DNA concentration was preadjusted to 10 ng/µL. Five microliters (50 ng) of the DNA solution was removed and mixed with 1.5 µL of 6× purple gel loading dye, no SDS, and loaded onto 1% agarose Tris Borate EDTA TBE gels. For denaturing gels, 5 µL (50 ng) of the DNA solution was removed and mixed with

15 μL of 0.4% denaturing buffer (0.53% sodium hydroxide, 10% glycerol, and 0.013% bromophenol blue) in an ice bath. The mixed DNA samples were denatured at 4 °C for 5 min and then immediately loaded onto a 1% agarose Tris Borate EDTA (TBE) gel. All gel electrophoresis was conducted at 90 V for 2 h (unless otherwise noted). The gel was stained with SYBR Gold (Invitrogen) for 2 h.

EndoIV Depurination Assay

For each condition, 200 ng of supercoiled pUC19 DNA (15.4 μM base pairs) was incubated with the indicated concentration of drug in 20 μL for 3 hours. Drug stock concentrations were made in DMSO such that each reaction contained a fixed 5% DMSO concentration. Reactions were conducted in 100 mM Tris buffer (pH 7.4). For each EndoIV reaction, 50 ng of processed DNA was mixed with 20 units of EndoIV in NEBuffer 3.1 (New England Biolabs), pH 7.9, in a total volume of 20 μL for 16−20 h (unless otherwise noted) at 37 °C. The NEBuffer 3.1 contained 100 mM sodium chloride, 50 mM Tris-HCl, 10 mM magnesium chloride, and 100 μg/mL BSA. For each negative control, 50 ng of processed DNA was mixed with NEBuffer 3.1, pH 7.9, in a total volume of 20 μL for 16−20 h (unless otherwise noted) at 37 °C. Following completion of the experiment, the DNA was stored at −20 °C before electrophoretic analysis.

Melting Temperature Assay

Linearized pUC19 DNA (750 ng), prepared as described above, was incubated with the indicated concentration of either MMS or KL-50 (**4a**) adjusted in a final volume of 18 μL in 100 mM Tris buffer (pH 7.4) for 3 h. Drug stock concentrations were made in DMSO such that each reaction contained a fixed 5% DMSO concentration. Afterwards, 1 μL each of 20x SYBR Green dye (Invitrogen) and 20x ROX reference dye (Invitrogen) was added and melting temperature analysis was run on a StepOnePlus RT PCR System (Applied Biosciences) to generate melting temperature curves.

Immunofluorescence Foci Assays

High-throughput immunofluorescence foci assays were performed at the Yale Center for Molecular Discovery (YCMD). Cells were seeded at 2000 cells/well in black polystyrene flat bottom 384-well plates (Greiner Bio-One) and allowed to adhere overnight. Compound addition was performed utilizing a Labcyte Echo 550 liquid handler (Beckman Coulter), with 6 replicates per test condition and 12 replicates per control condition. Following drug incubation, cells were fixed and stained for phospho-SER139-H2AX (γH2AX), 53BP1, or phospho-SER33-RPA2 (pRPA) as follows.

> *γH2AX protocol:* Cells were fixed with 4% paraformaldehyde in 1X PBS for 15 min, washed twice with 1X PBS, incubated in extraction buffer (0.5% Triton X-100 in 1X PBS) for 10 min, washed twice with 1X PBS, and incubated in blocking buffer (Blocker Casein in PBS, Thermo Scientific + 5% goat serum, Life Technologies) for 1 h. Mouse anti-phospho-histone H2A.X (Ser139) antibody (clone JBW301, Millipore, 05-636) was added 1/1000 in blocking buffer at 4 ºC overnight. After washing with 1X PBS, cells were incubated with goat anti-mouse IgG (H+L) highly cross-adsorbed secondary antibody, Alexa Fluor 647 (Invitrogen, A-21236) 1/500 and with 1 μg/mL Hoechst nucleic acid dye in blocking buffer for 2 h, and then washed with 1X PBS.

53BP1 protocol: Assay was performed as previously described (*66*). Cells were fixed with 4% paraformaldehyde + 0.02% Triton X-100 in 1X PBS for 20 minutes, washed twice with 1X PBS, and incubated in blocking buffer (10% FBS, 0.5% Triton X-100 in 1X PBS) for 1 h. Rabbit anti-53BP1 antibody (Novus Biologicals, NB100-904) was added 1/1000 in blocking buffer at 4 ºC overnight. After washing with 1X PBS, cells were incubated with goat anti-rabbit IgG (H+L) highly cross-adsorbed secondary antibody, Alexa Fluor 647 (Invitrogen, A-21245) 1/500 and with 1 µg/mL Hoechst nucleic acid dye in blocking buffer for 2 h, and then washed with 1X PBS.

pRPA protocol: Cells were washed twice with 1X PBS on ice, incubated in extraction buffer (0.5% Triton X-100 in 1X PBS) for 5 min on ice, fixed with 3% paraformaldehyde + 2% sucrose in 1X PBS for 15 min at 23 ºC, incubated again in extraction buffer for 5 min on ice, and incubated in blocking buffer (2% BSA, 10% milk, 0.1% Triton X-100 in 1X PBS) for 1 h at 23 ºC. Rabbit anti-phospho-RPA2 (S33) antibody (Bethyl Laboratories, A300-246A) was added 1/1000 in blocking buffer at 4 ºC overnight. After washing 4 times with IF wash buffer (0.1% Triton X-100 in 1X PBS), cells were incubated with goat anti-rabbit IgG (H+L) highly cross-adsorbed secondary antibody, Alexa Fluor 647 (Invitrogen, A-21245) 1/500 and with 1 µg/mL Hoechst nucleic acid dye in blocking buffer for 1 h at 37 ºC. Cells were washed twice with IF wash buffer and twice with 1X PBS.

Imaging was performed on an InCell Analyzer 2200 Imaging System (GE Corporation) at 40X magnification. Twenty fields-of-view were captured per well. Foci analysis was performed using InCell Analyzer software (GE Corporation) as previously described (*65*). Outer wells were excluded from analysis to limit variation due to edge effects.

Additional small scale immunofluorescence assays used for extended time course analysis of γH2AX foci were performed in Millicell EZ_{SLIDE} 8-well chamber slides (Millipore). Cells were seeded at 10,000 cells/well and allowed to adhere overnight. Following drug treatment, cells were fixed and stained for γH2AX as described above, without the addition of Hoechst dye. Slides were mounted with Vectashield Antifade Mounting Medium with DAPI (Vector Laboratories). Imaging was performed on a Keyence BZ-X800 fluorescence microscope at 40X magnification. Nine adjacent fields-of-view were captured per well and stitched together using a Fiji/ImageJ software plugin. Foci analysis was performed using Focinator v2 software (*66*, *67*).

Cell Cycle Analysis

Cell cycle analysis was performed using integrated Hoechst nucleic acid dye fluorescence intensity as previously described (*68*). Briefly, integrated Hoechst fluorescence intensity was $\log_2$ transformed and histograms from DMSO-treated cells were used to identify the centers of the 2N and 4N DNA peaks. These values were used to normalize the 2N DNA peak to 1 and the 4N DNA peak to 2. Cells were then classified by normalized $\log_2$ DNA content as G1 (0.75–1.25), S (1.25–1.75), or G2 (1.75–2.5) phase cells. The percentage of cells within each phase of the cell cycle was determined for each treatment condition. The three sets of Hoechst-stained cells corresponding to the three separate DNA foci stains were treated as three independent analyses.

Micronuclei Analysis

An automated image analysis pipeline was developed by YCMD using InCell Analyzer software to quantify micronuclei formation. Nuclei and micronuclei were segmented based on Hoechst nucleic acid dye staining channel. A perinuclear margin was applied around the nuclei to approximate the extent of the cytoplasm and identify micronuclei associated with the parent nucleus. Cells with nuclei associated with at least 1 micronucleus were considered positive.

Animal Use

All animal use was in accordance with the guidelines of the Animal Care and Use Committee (IACUC) of Yale University (Yale University IACUC, Protocol # 2021-20071) and conformed to the recommendations in the Guide for the Care and Use of Laboratory Animals (Institute of Laboratory Animal Resources, National Research Council, National Academy of Sciences, 1996).

Mouse Protocols for Flank Studies

A mouse tumor model was established by subcutaneously implanting human LN229 (MGMT–/MMR+) or LN229 (MGMT–/MMR–) cells. Cells were cultured as a monolayer in DMEM +10% FBS (Thermo Fisher) at 37 °C in a humidified atmosphere with 5% CO_2 and passaged between one and three days prior to implantation and media was replaced every 2-3 days as needed to maintain cell viability. Cells were not allowed to exceed 80% confluency. On the day of implantation, cells were trypsinized, washed with complete media and pelleted by centrifugation at 1200 rpm for 5 minutes. The supernatant was decanted, and cells were washed three times with sterile PBS and pelleted by centrifugation. During the final centrifugation, viability was determined using trypan blue exclusion. Cells were resuspended in sterile PBS and diluted 1:1 in Matrigel (Corning, Cat #47743-716) for a final concentration of 5×10^6 cells/ 100 µL. 5 million cells were injected into the flank of female nude mice (Envigo, Hsd:Athymic Nude-Foxn1^{nu}, 3-4 weeks age, 15 g). Once tumors reached a minimum volume of 100 mm^3, mice were randomized and administered either KL-50 (**4a;** 5 mg/kg MWF × 3 weeks), TMZ (**1a;** 5 mg/kg MWF × 3 weeks), or vehicle (10% cyclodextrin) by oral gavage. Caliper measurements were obtained during the dosing period and at least two weeks following treatment. Mice with tumors sizes >2 SDs from the group average by the first treatment day or whose tumors failed to implant were excluded from the study. Mice were euthanized if body weight loss exceeded 20% or if tumor volume increased to greater than 2000 mm^3. Kaplan–Meier analysis was used to evaluate survival rate based on death or removal from study.

In a second study, mice were randomized and administered either KL-50 (**4a**) or vehicle (10% cyclodextrin) by oral gavage or intraperitoneal injection on either M–F × 1 or MWF × 3 cycles at 5, 15, or 25 mg/kg. Caliper measurements were obtained during the dosing period and at least two weeks following treatment. Mice were euthanized if body weight loss exceeded 20% or if tumor volume increased to greater than 2000 mm^3. The mice with the single largest and single smallest tumor growth in each group, corresponding to approximately 1 SD from the mean, or whose tumors failed to implant were excluded from analysis.

The third study involved MGMT–/MMR+ and MGMT–/MSH6– (shMSH6) LN229 cells. Mice tumors were allowed to grow to a larger average starting volume of ~350 mm^3 before they were randomized and administered either KL-50 (**4a;** 25 mg/kg MWF × 3 weeks) or vehicle (10% cyclodextrin) by oral gavage. Caliper measurements were obtained during the dosing period and

at least two weeks following treatment. Mice were euthanized if body weight loss exceeded 20% or if tumor volume increased to greater than 3000 mm^3.

Mouse Protocol for Intracranial Study

LN229 MGMT–/MMR– cells stably expressing firefly luciferase (lentivirus-plasmids from Cellomics Technology; PLV-10003), were injected intracranially using a stereotactic injector. Briefly, 1.5 million cells in 5 μl PBS were injected into the brain and the mice were imaged weekly using the IVIS Spectrum In Vivo Imaging System (PerkinElmer) according to the manufacturer's protocol. Images were taken on a weekly basis and acquired 10 min post intraperitoneal injection with d-luciferin (150 mg/kg of animal mass). Tumors were allowed to grow to an average of 1.0 × 10^8 RLU before randomization and treated with 5 continuous days of PO treatment with 10% cyclodextrin vehicle control, TMZ (**1a**, 25 mg/kg M–F × 1 week) or KL-50 (**4a**, 25 mg/kg M–F × 1 week). Quantification of BLI flux (photons/sec) was made through the identification of a region of interest (ROI) for each tumor.

Statistical Analysis

Statistical analysis was performed using GraphPad Prism software. Data are presented as mean or median ± SD or SEM as indicated. For *in vitro* short-term growth delay experiments, IC_{50} values were determined from the nonlinear regression equation, [inhibitor] vs normalized response with variable slope. For micronuclei assays, comparisons were made with one-way ANOVA and Sidak correction for multiple comparisons. For xenograft growth delay experiments, comparisons were made with Mann-Whitney test (for comparison of 2 groups) or Kruskal-Wallis test with FDR-adjusted p-values with Q set to 5% (for comparison of ≥ 3 groups). For xenograft survival analysis, Kaplan–Meier analysis was used to evaluate survival rate based on death or removal from study when body weight loss exceeded 20% of initial body weight, and statistical comparisons were made by log-rank (Mantel-Cox) test with Bonferroni correction for multiple comparisons.

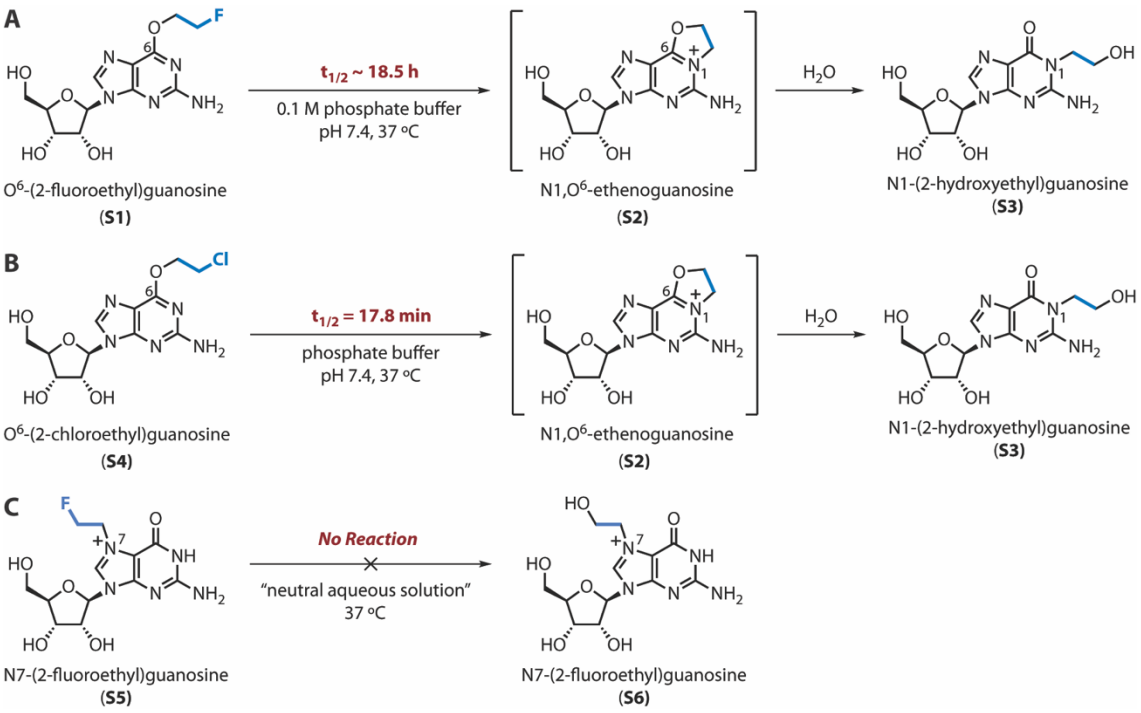

Fig. S1.

Literature precedent for the hydrolysis of various 2-haloethylguanosine lesions. (**A**) Kinetics of the hydrolysis of *O*^{6}-(2-fluoroethylguanosine) (**S1**) at pH 7.4 and 37 ºC as reported by Tong et al. (*19*). (**B**) Kinetics of the hydrolysis of *O*^{6}-(2-chloroethylguanosine) (**S4**) at pH 7.4 and 37 ºC as reported by Parker et al. (*44*). (**C**) Failed hydrolysis of *N*7-(2-fluoroethyl)guanosine (**S5**) with "extensive incubation of [**S5**] at 37 º [C] in neutral aqueous solution" as reported by Ludlum et al. (*45*).

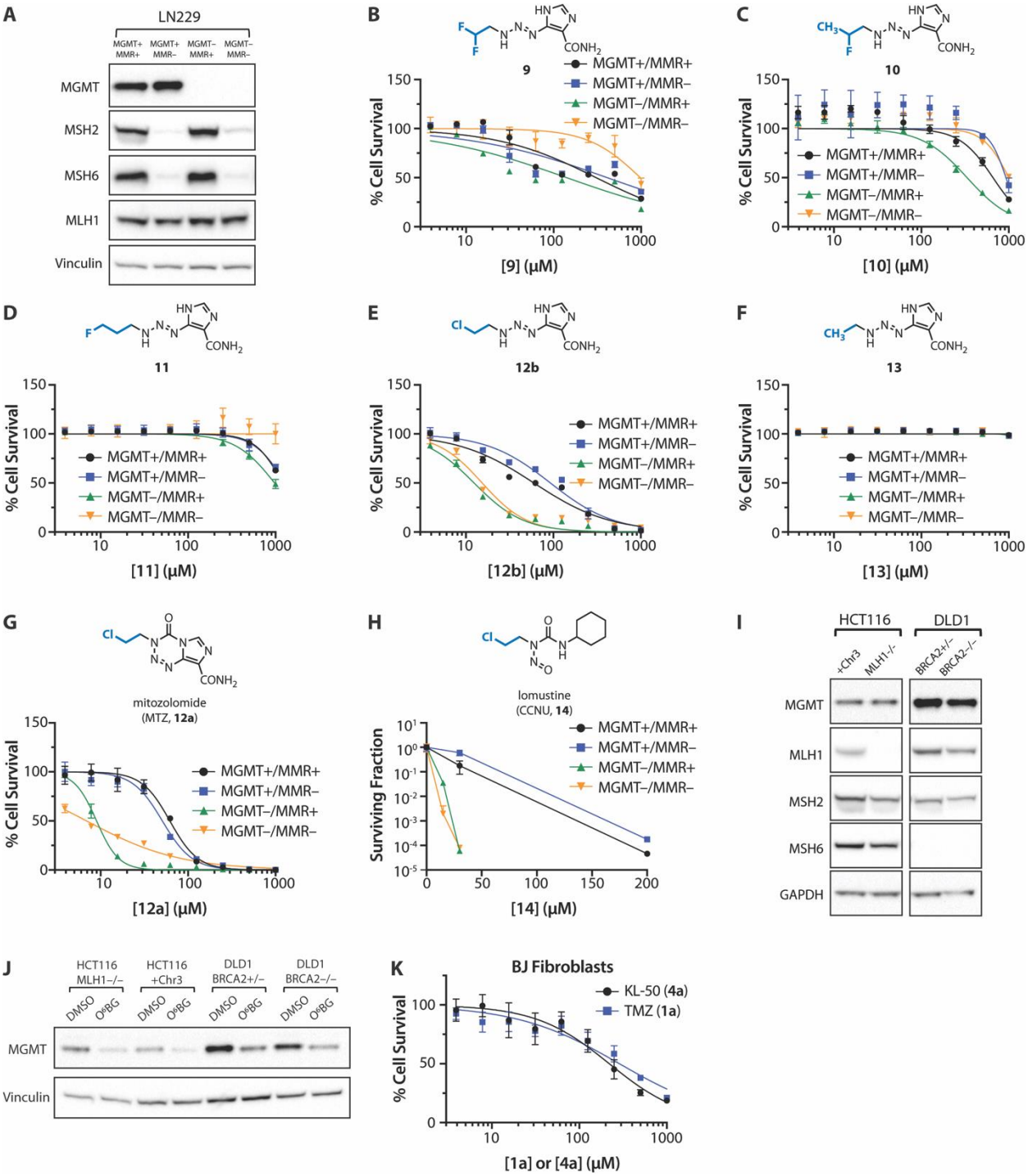

Fig. S2.

Additional analysis of TMZ (1a) derivatives in MGMT+/–, MMR+/– cell models. (**A**) Western blotting performed in LN229 MGMT–/MMR+ parental line, and cells complemented with wildtype MGMT (MGMT+/MMR+) and/or stable expression of MSH2 shRNA (MGMT+/MMR– and MGMT–/MMR–). MSH6 expression is reduced in these lines due to destabilization in the setting of loss of its heterodimeric partner MSH2. MLH1 expression is not affected by MSH2 knockdown. Vinculin serves as loading control. (**B**, **C**, **D**, **E**, **F**, and **G**) Short-term viability assay

curves for compounds **9**, **10**, **11**, **12b**, **13**, and **12a** in LN229 MGMT+/–, MMR+/– cells. (**H**) Clonogenic survival curves for lomustine (**14**) in LN229 MGMT+/–, MMR+/– cells. (**I**) Western blotting in HCT116 and DLD1 cells. HCT116 MLH1–/– and +Chr3 lines demonstrate re-expression of MLH1 and similar levels of MGMT and other MMR proteins. DLD1 BRCA2+/– and BRCA2–/– cells have known loss of MSH6 but comparable levels of MGMT and other MMR protein expression. GAPDH serves as loading control. (**J**) Western blotting performed in HCT116 MLH1–/– and +Chr3 and DLD1 BRCA2+/– and BRCA2–/– cells after exposure to 0.01% DMSO or 10 μM O^6BG for 24 h, demonstrating O^6BG-induced MGMT depletion. Vinculin serves as loading control. (**K**) Short-term cell viability curves for KL-50 (**4a**) and TMZ (**1a**) in BJ fibroblast cells. For (B), (C), (D), (E), (F), (G), (H), and (K), *points*, mean; *error bars*, SD; $n = 3$ technical replicates.

A

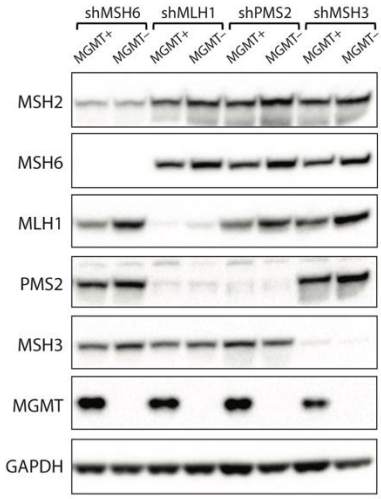

B

IC_{50} (μM) Values of TMZ (1a) and KL-50 (4a) against LN229 MGMT+/– cell lines, +/– shRNA

shRNA	Compound	MGMT+ MMR+	MGMT+ MMR–	MGMT– MMR+	MGMT– MMR–	MGMT TI [a]	MMR RI [b]
None	TMZ (1a)	697 ± 60	---	5.1 ± 0.8	---	137	---
None	KL-50 (4a)	285 ± 46	---	13.2 ± 0.8	---	22	---
shMSH6	TMZ (1a)	---	929 ± 201	---	950 ± 68	---	186
shMSH6	KL-50 (4a)	---	362 ± 41	---	6.6 ± 0.4	---	0.5
shMLH1	TMZ (1a)	---	769 ± 100	---	917 ± 85	---	180
shMLH1	KL-50 (4a)	---	252 ± 28	---	7.8 ± 0.3	---	0.6
shPMS2	TMZ (1a)	---	700 ± 58	---	921 ± 190	---	181
shPMS2	KL-50 (4a)	---	215 ± 16	---	5.4 ± 0.3	---	0.4
shMSH3	TMZ (1a)	---	649 ± 32	---	3.1 ± 0.6	---	0.6
shMSH3	KL-50 (4a)	---	328 ± 26	---	7.9 ± 0.3	---	0.6

C

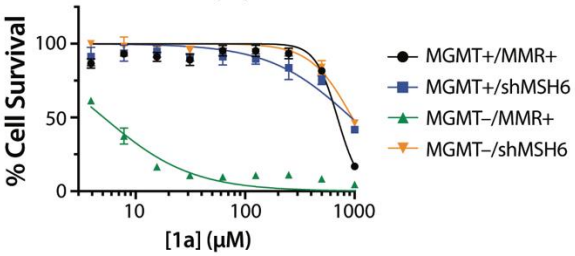

D

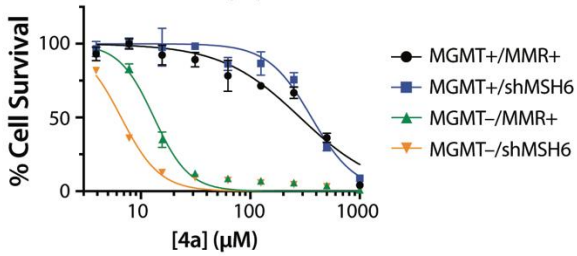

E

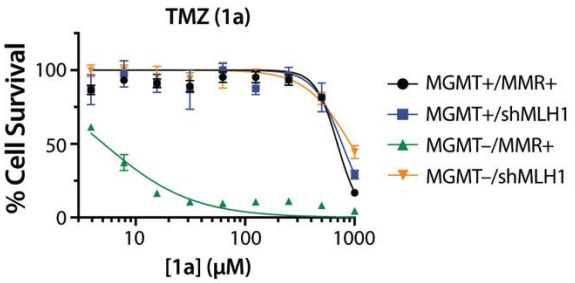

F

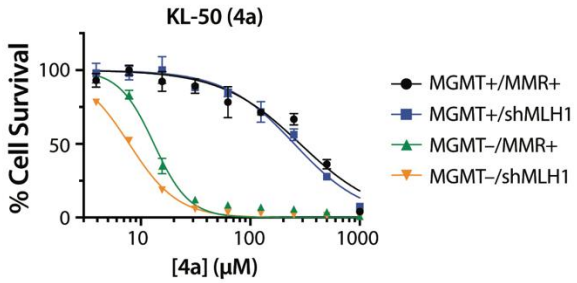

G

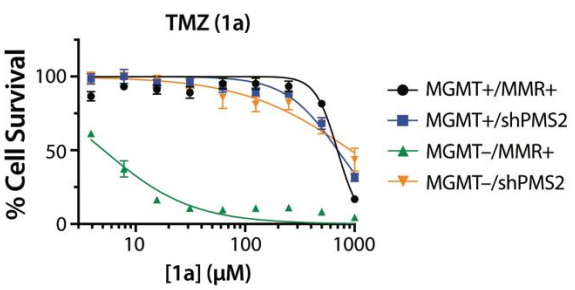

H

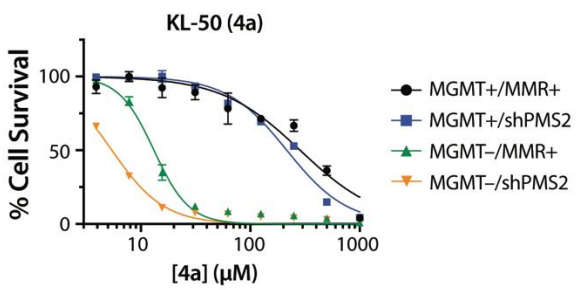

I

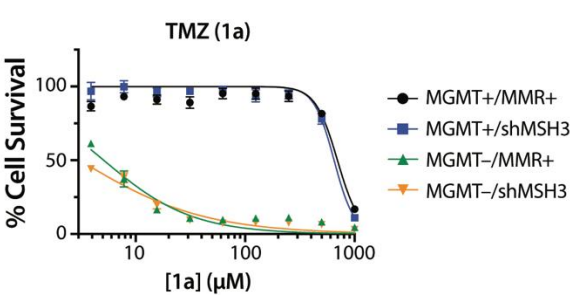

J

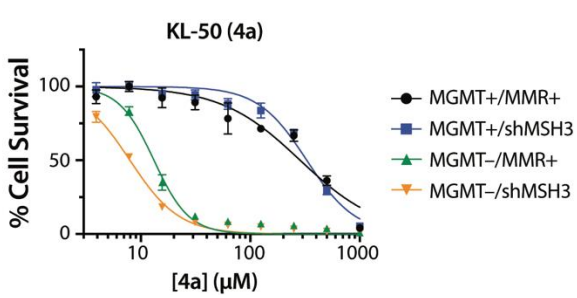

Fig. S3.

KL-50 (4a) is effective in TMZ (1a)-resistant cells lacking other MMR proteins. (**A**) Western blotting performed in LN229 MGMT+/– cells with stable expression of shRNA targeting MSH6, MLH1, PMS2, or MSH3 to confirm depletion of the shRNA targets. In shMSH6 cells, there is reduced expression of MSH2, and in shMLH1 cells, there is loss of PMS2, due to destabilization in the setting of loss of their heterodimeric partners. GAPDH serves as loading control. (**B**) IC_{50} values derived from short-term viability assays in LN229 MGMT+/– cells lines, +/–shRNA, treated with TMZ (**1a**) or KL-50 (**4a**). [a]MGMT TI (therapeutic index) = IC_{50} (MGMT+/MMR+) divided by IC_{50} (MGMT–/MMR+). [b]MMR RI (resistance index) = IC_{50} (MGMT–/MMR–) divided by IC_{50} (MGMT–/MMR+). (**C**) Short-term viability assay curves for TMZ (**1a**) in LN229 MGMT+/–, MMR+/shMSH6 cells. (**D**) Short-term viability assay curves for KL-50 (**4a**) in LN229 MGMT+/–, MMR+/shMSH6 cells. (**E**) Short-term viability assay curves for TMZ (**1a**) in LN229 MGMT+/–, MMR+/shMLH1 cells. (**F**) Short-term viability assay curves for KL-50 (**4a**) in LN229 MGMT+/–, MMR+/shMLH1 cells. (**G**) Short-term viability assay curves for TMZ (**1a**) in LN229 MGMT+/–, MMR+/shPMS2 cells. (**H**) Short-term viability assay curves for KL-50 (**4a**) in LN229 MGMT+/–, MMR+/shPMS2 cells. (**I**) Short-term viability assay curves for TMZ (**1a**) in LN229 MGMT+/–, MMR+/shMSH3 cells. (**J**) Short-term viability assay curves for KL-50 (**4a**) in LN229 MGMT+/–, MMR+/shMSH3 cells. For (C), (D), (E), (F), (G), (H), (I), and (J), *points*, mean; *error bars*, SD; $n = 3$ technical replicates. The same MMR+ data have been replotted in (C), (E), (G), and (I) and in (D), (F), (H), and (J).

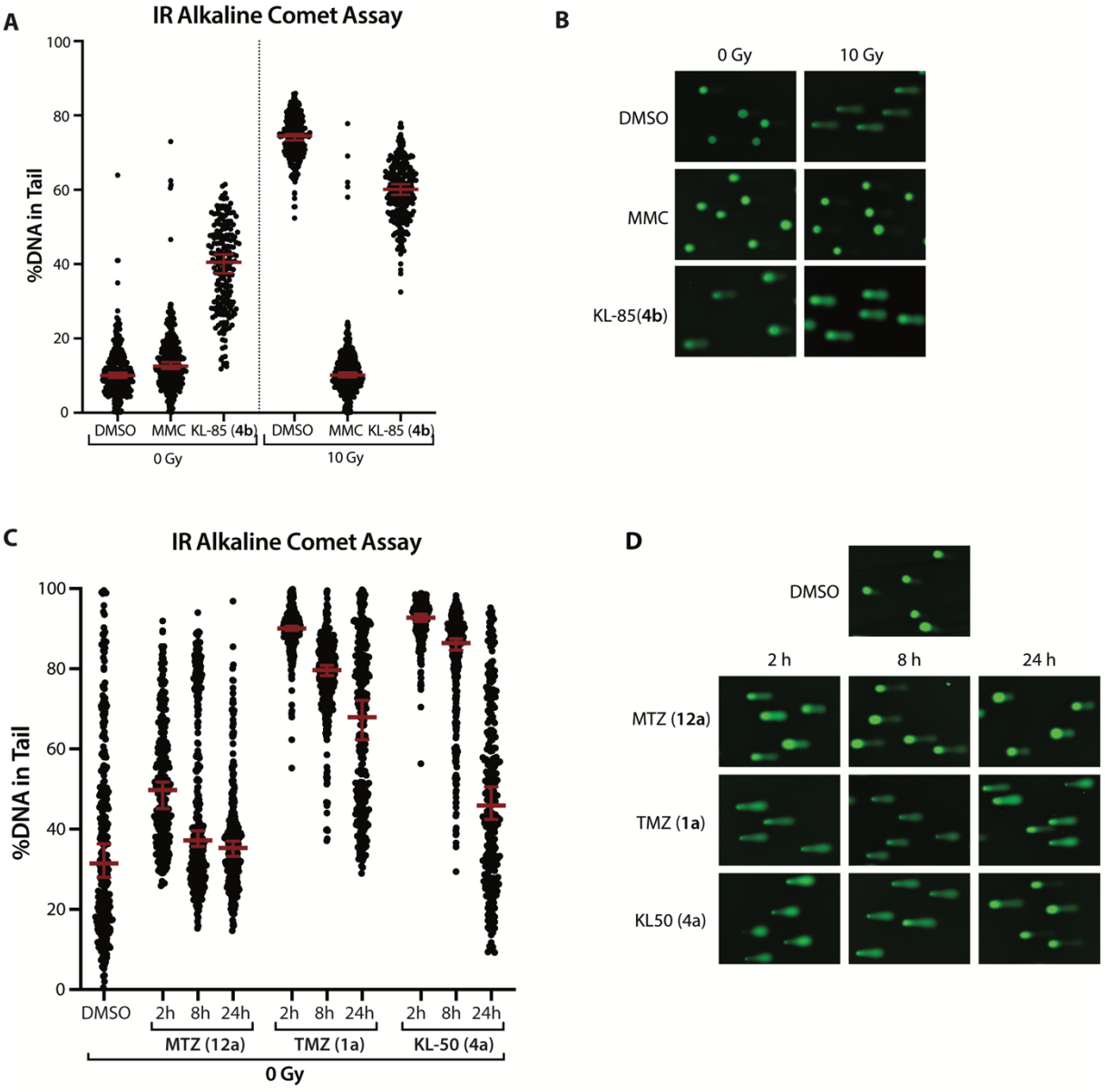

E

ICL Band Quantification (related to Fig. 3F)			
	Background	KL-50 (4a)	
6 h	129	131	
12 h	128	132	
24 h	127	134	
36 h	128	131	
Average	128	132	p=0.0027

Fig. S4.

Supplementary IR alkaline comet assay and denaturing gel electrophoresis data. (**A**) Scatter dot plots of the %DNA in tail upon single cell alkaline gel electrophoresis performed on LN229 MGMT–/MMR+ cells treated with 0.1% DMSO control or 200 μM KL-85 (**4b**) for 24 h or with 50 μM MMC for 2 h. After cell lysis, comet slides were irradiated with 0 or 10 Gy prior to alkaline

electrophoresis. *Line*s, median; *error bars*, 95% CI; $n \geq 160$. (**B**) Representative comet images from (A). (**C**) Scatter dot plots of the %DNA in tail upon single cell alkaline gel electrophoresis performed on LN229 MGMT–/MMR– cells treated with 0.2% DMSO control, 200 μM MTZ (**12a**), 200 μM TMZ (**1a**), or 200 μM KL-50 (**4a**) for 2, 8, or 24 h. Corresponding samples treated with 10 Gy IR are shown in Fig. 3C. *Line*s, median; *error bars*, 95% CI; $n \geq 230$. **(D**) Representative comet images from (C). (**E**) Quantification of the cross-linked bands from the gel in Fig. 3F, performed by measuring pixel intensity in the area above the expected cross-linked DNA band (background) and the expected area of cross-linked DNA band of the same lane (KL-50, **4a**). Unpaired t-test was used to analyze statistical difference between pixel intensities.

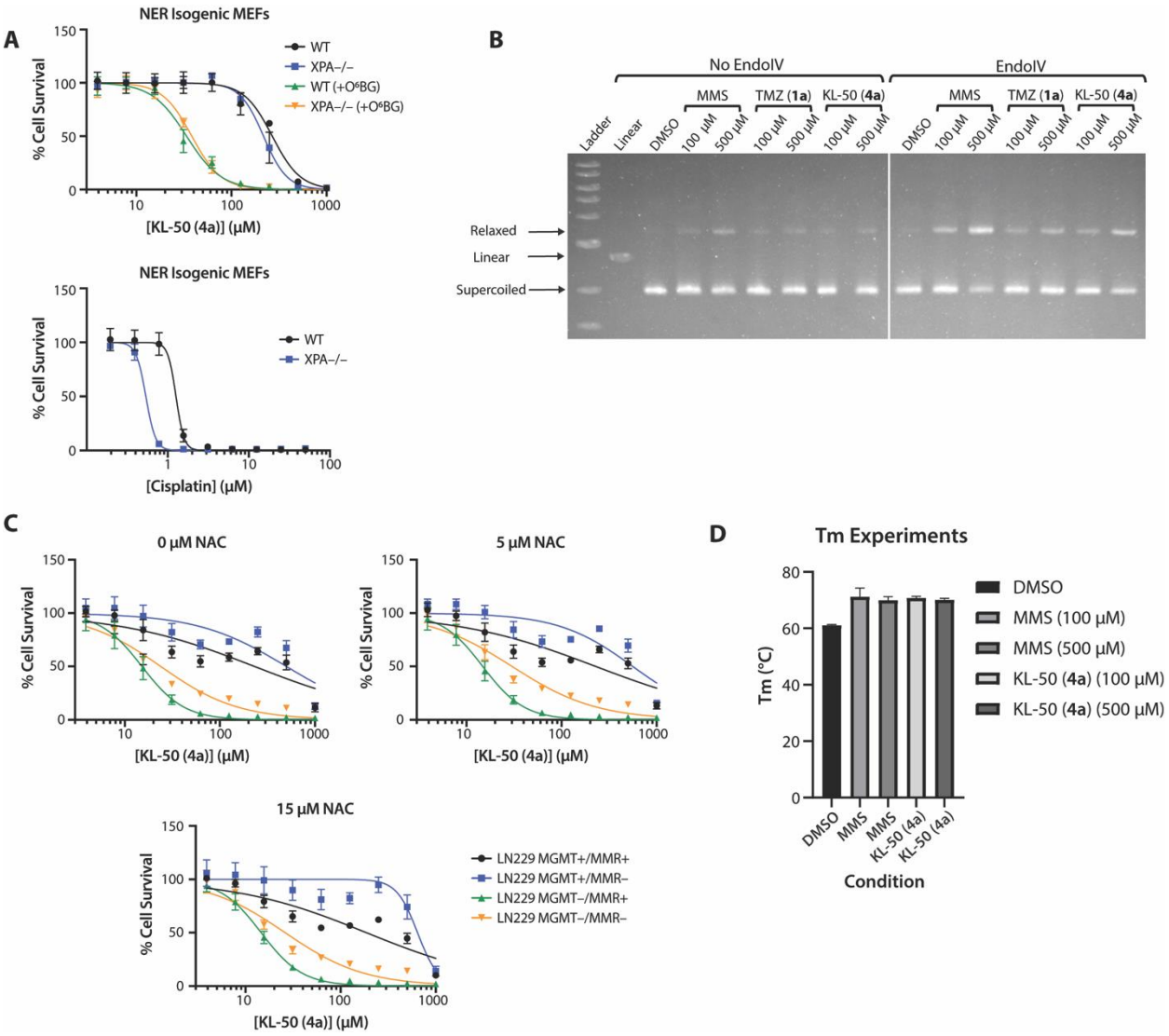

Fig. S5.

NER, BER, ROS, and altered DNA melting point do not play a major role in the mechanism of KL-50 (4a). (**A**) Short-term cell viability assays in both WT and XPA-deficient MEFs demonstrating the absence of additional sensitivity to KL-50 (**4a**) in NER compromised XPA-deficient cells ±MGMT depletion with O^6BG, in contrast to cisplatin as positive control. (**B**) EndoIV depurination assay utilizing supercoiled pUC19 plasmid DNA assessing both spontaneous and enzymatically catalyzed SSB formation resulting from depurination post-treatment, demonstrating comparable levels of depurination and SSB formation by KL-50 (**4a**) and TMZ (**1a**). (**C**) Short-term cell viability assays in LN229 MGMT+/– , MMR+/– isogenic lines pre-treated with increasing concentrations of the ROS scavenger NAC did not result in rescue of KL-50 (**4a**) toxicity. (**D**) Melting temperature experiments in linearized pUC19 plasmid DNA treated with 100 or 500 μM of MMS or KL-50 (**4a**) for 3 h resulted in comparable changes in measured DNA melting temperature. *Columns*, mean; *error bars*, SD; *n* = 2 independent analyses. For (A) and (C), *points*, mean; *error bars*, SD; *n* = 3 technical replicates.

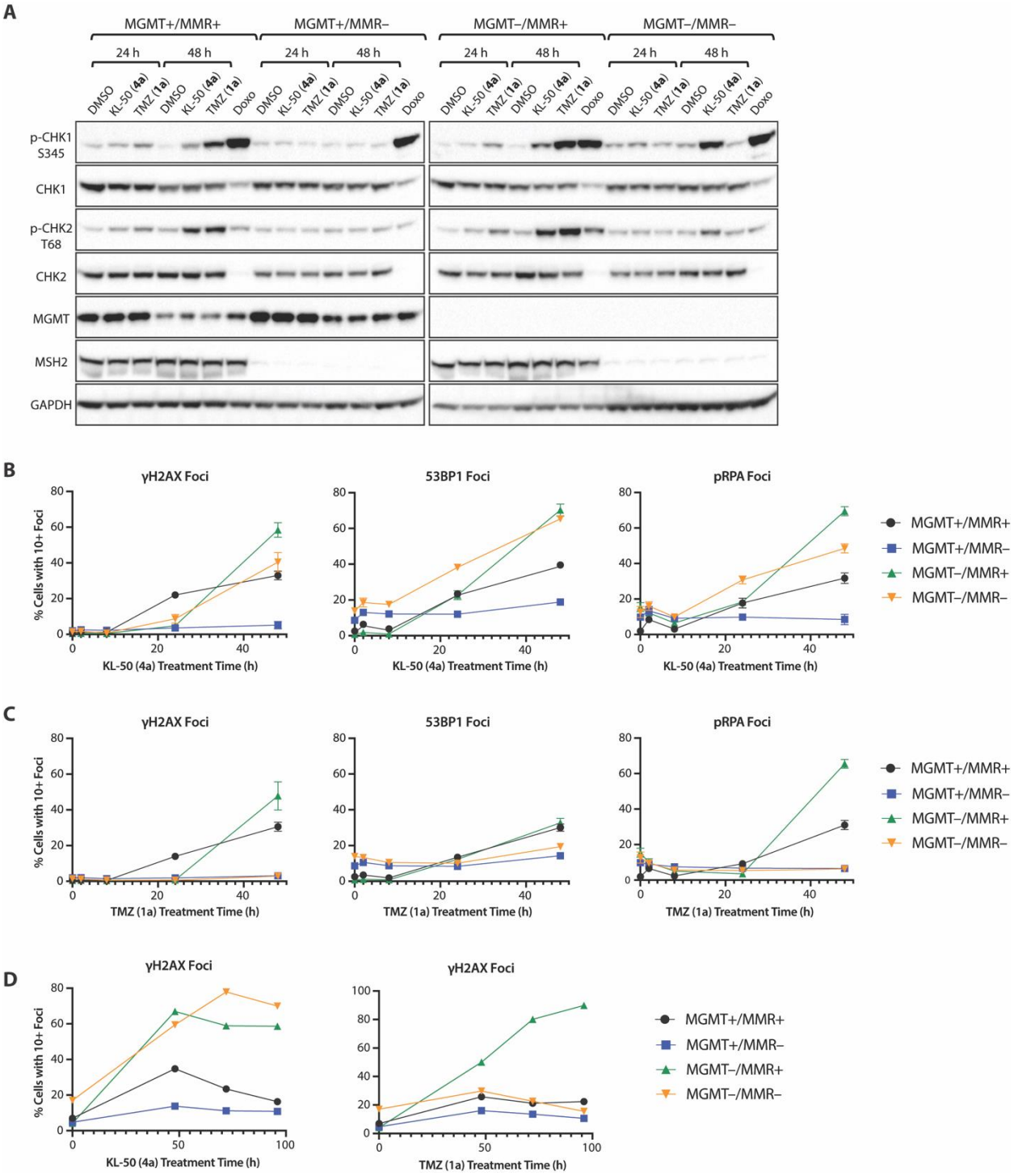

Fig. S6.

KL-50 (4a) induces activation of the ATR-CHK1 and ATM-CHK2 signaling axes and delayed DDR foci formation in MGMT-deficient cells, independent of MMR status. (**A**) Western blotting performed in LN229 MGMT+/–, MMR+/– cells following treatment with 20 μM KL-50 (**4a**) or TMZ (**1a**) for 24 or 48 h. Treatment with 1 μM doxorubicin for 24 h (Doxo) served as a positive control for p-CHK1 activation. (**B** and **C**) Phospho-SER139-H2AX (γH2AX),

53BP1, and phospho-SER33-RPA2 (pRPA) foci levels over time following treatment with KL-50 (**4a**; 20 μM) (B) or TMZ (**1a**; 20 μM) (C) for 0, 2, 8, 24, or 48 h in LN229 MGMT+/–, MMR+/– cells. *Points*, mean % cells with ≥10 foci; *error bars*, SD; $n \geq 5$ technical replicates. (**D**) Extended time course of γH2AX foci levels following treatment with KL-50 (**4a**; 20 μM) or TMZ (**1a**; 20 μM) for 0, 48, 72, or 96 h in LN229 MGMT+/–, MMR+/– cells. *Points*, % cells with ≥10 foci, n ≥250 cells per condition.

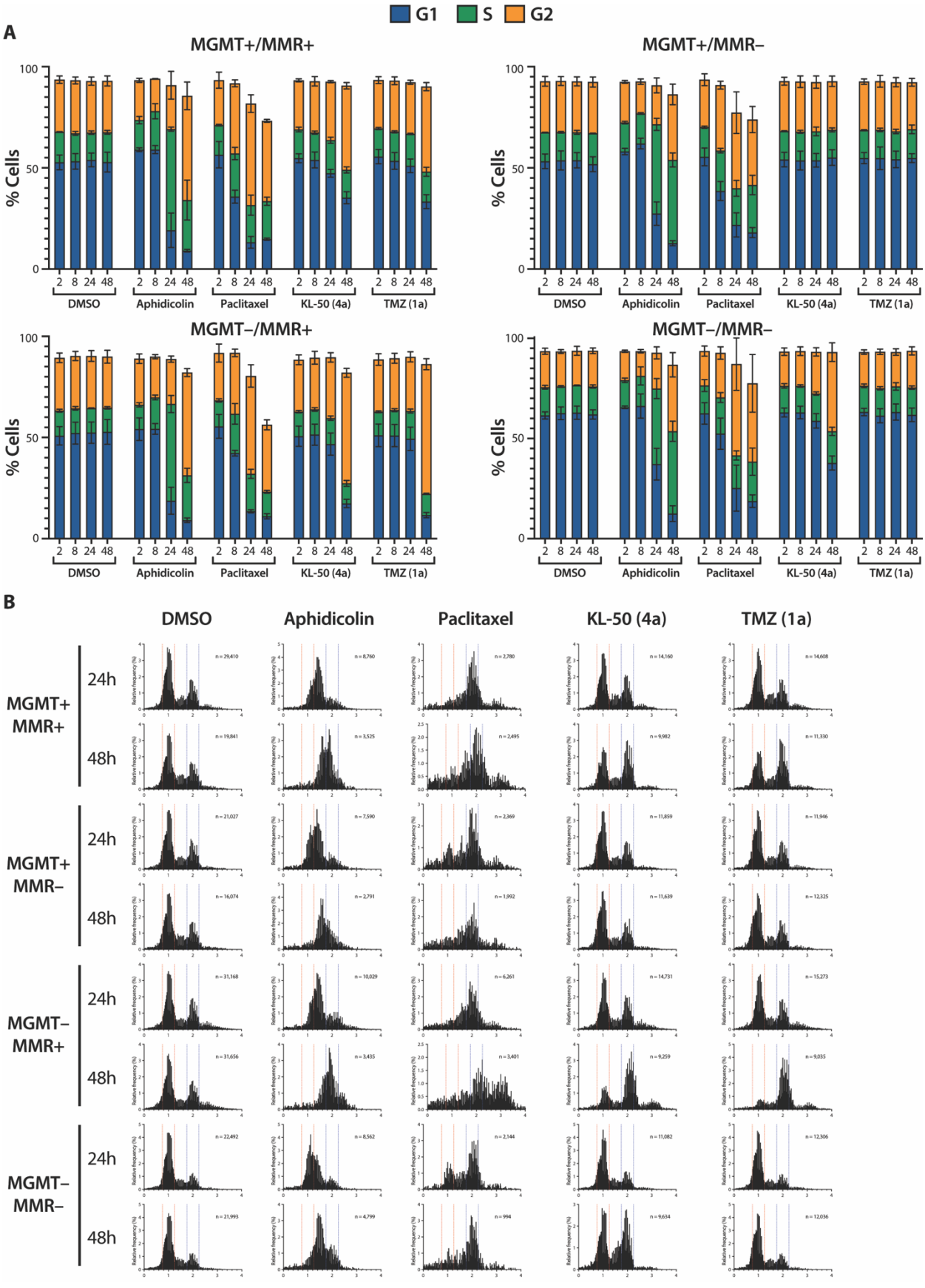
A
G1
S
G2
MGMT+/MMR+
MGMT+/MMR–
MGMT–/MMR+
MGMT–/MMR–
% Cells
100
50
0
2 8 24 48
DMSO
Aphidicolin
Paclitaxel
KL-50 (4a)
TMZ (1a)
B
DMSO
Aphidicolin
Paclitaxel
KL-50 (4a)
TMZ (1a)
MGMT+ MMR+
MGMT+ MMR–
MGMT– MMR+
MGMT– MMR–
24h
48h
Relative frequency (%)
n = 29,410
n = 8,760
n = 2,780
n = 14,160
n = 14,608
n = 19,841
n = 3,525
n = 2,495
n = 9,982
n = 11,330
n = 21,027
n = 7,590
n = 2,369
n = 11,859
n = 11,946
n = 16,074
n = 2,791
n = 1,992
n = 11,639
n = 12,325
n = 31,168
n = 10,029
n = 6,261
n = 14,731
n = 15,273
n = 31,656
n = 3,435
n = 3,401
n = 9,259
n = 9,035
n = 22,492
n = 8,562
n = 2,144
n = 11,082
n = 12,306
n = 21,993
n = 4,799
n = 994
n = 9,634
n = 12,036

Fig. S7.

Supplementary cell cycle analysis data. (**A**) Time course analysis of cell cycle distribution measured using integrated nuclear (Hoechst) staining intensity after treatment of LN229 MGMT+/–, MMR+/– cells with KL-50 (**4a**; 20 μM) or TMZ (**1a**; 20 μM) for 2, 8, 24, or 48 h. DMSO (0.1%) serves as negative control and aphidicolin (10 μM) and paclitaxel (1 μM) serve as positive controls for S-phase and G2-phase arrest, respectively (*68*). *Columns*, mean; *error bars*, SD; $n = 3$ independent analyses. (**B**) Representative histograms showing DNA content distribution from 24 h and 48 h treatment conditions as quantified in (A).

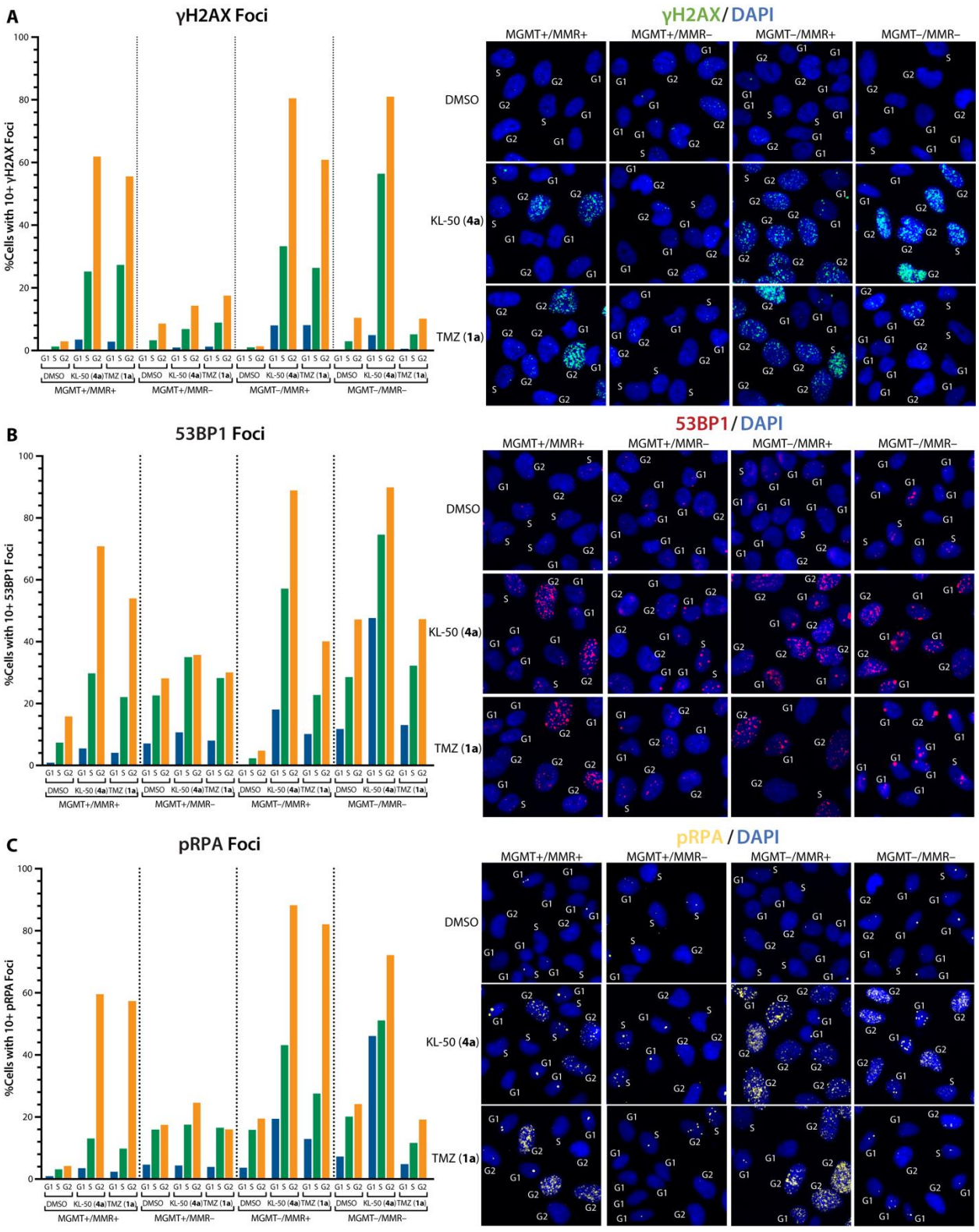

Fig. S8.

KL-50 (4a) induces DDR foci formation primarily in S and G2 cell cycle phases, and to lesser extent, in MGMT– G1 phase cells. (**A**) Phospho-SER139-H2AX (γH2AX) foci levels in LN229

MGMT+/–, MMR+/– cells in G1, S, and G2 cell cycle phases after treatment with 0.1% DMSO control, KL-50 (**4a**; 20 μM), or TMZ (**1a**; 20 μM) for 48 h. Representative foci images with nuclei labeled as G1, S, or G2 phase cells based on Hoechst staining intensity are shown on the right. (**B**) 53BP1 foci levels and representative foci images in cells treated as in (A). (**C**) Phospho-SER33-RPA2 (pRPA) foci levels and representative foci images in cells treated as in (A). For (A), (B), and (C), *points*, % cells with ≥10 foci; n ≥500 cells per condition and cell cycle phase.

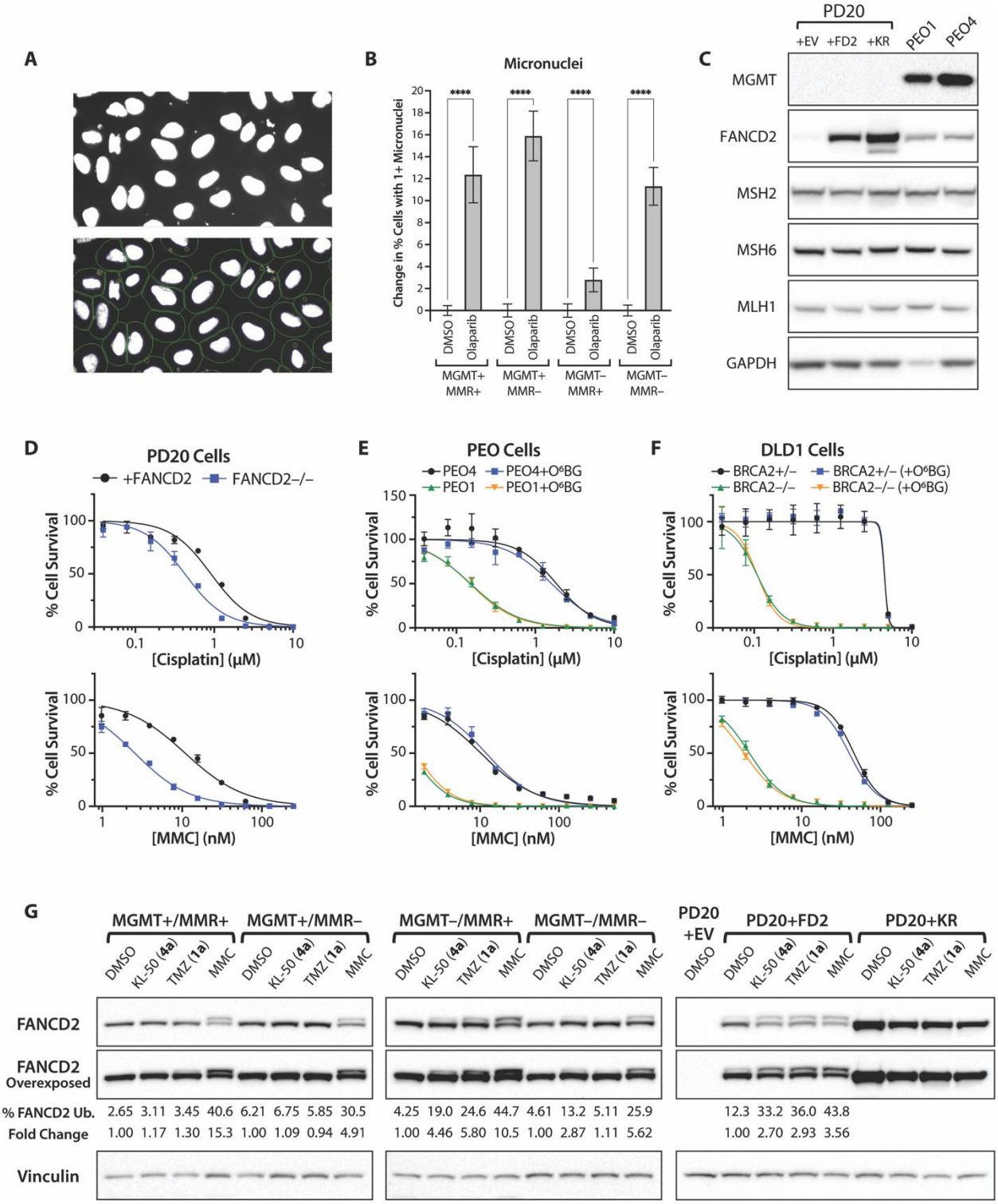

Fig. S9.

Validation of micronuclei analysis, ICL sensitivity in FANCD2–/– and BRCA2–/– cell models, and demonstration of FANCD2 ubiquitination induced by KL-50 (4a). (**A**) Representative images of micronuclei identification. (**B**) Validation of micronuclei identification

using olaparib as positive control. Change in percent cells with ≥1 micronuclei from baseline (DMSO control) after treatment with olaparib (10 μM) for 48 h in LN229 MGMT+/–, MMR+/– cells. *Columns*, mean; *error bars*, SD; *n* ≥15 technical replicates; **** p <0.0001. (**C**) Western blotting performed in PD20 cells complemented with empty vector (EV), wildtype FANCD2 (WT), or ubiquitination-mutant FANCD2 (KR), demonstrating loss of MGMT in PD20 cells and comparable expression of MMR proteins. Western blotting in PEO1 BRCA2–/– and PEO4 BRCA2+ cells demonstrates intact expression of MGMT and MMR proteins. (**D**) Short-term viability assay curves for cisplatin and mitomycin (MMC) in PD20 cells, deficient in FANCD2 (FANCD2–/–) or complemented with FANCD2 (+FANCD2), demonstrating hypersensitivity to crosslinking agents in FANCD2–/– cells. (**E**) Short-term viability assay curves for cisplatin and MMC in PEO4 (BRCA2+) and PEO1 (BRCA2–/–) cells pre-treated with 0.01% DMSO control or 10 μM O^6BG (+O^6BG) for 1 h prior to cisplatin or MMC addition, demonstrating hypersensitivity of PEO1 BRCA2–/– cells to crosslinking agents independent of MGMT depletion. (**F**) Short-term viability assay curves for cisplatin and MMC in DLD1 BRCA2+/– and BRCA2–/– cells pre-treated with 0.01% DMSO control or 10 μM O^6BG (+O^6BG) for 1 h prior to cisplatin or MMC addition, demonstrating hypersensitivity of DLD1 BRCA2–/– cells to crosslinking agents independent of MGMT depletion. (**G**) Western blot analysis of FANCD2 ubiquitination in LN229 MGMT+/–, MMR+/– cells and PD20 FANCD2-deficient cells, complemented with empty vector (FANCD2+EV), wildtype FANCD2 (PD20+FD2) or ubiquitination-mutant FANCD2 (PD20+KR). The % FANCD2 ubiquitination (% FANCD2 Ub.) is quantified as the background-corrected integrated band intensity of the upper band divided by the sum of the background-corrected integrated band intensities of the upper and lower bands. The fold change in % FANCD2 ubiquitination is presented for each cell line relative to DMSO-treated cells. Vinculin serves as loading control. For (D), (E), and (F), *points*, mean; *error bars*, SD; *n* = 3 technical replicates.

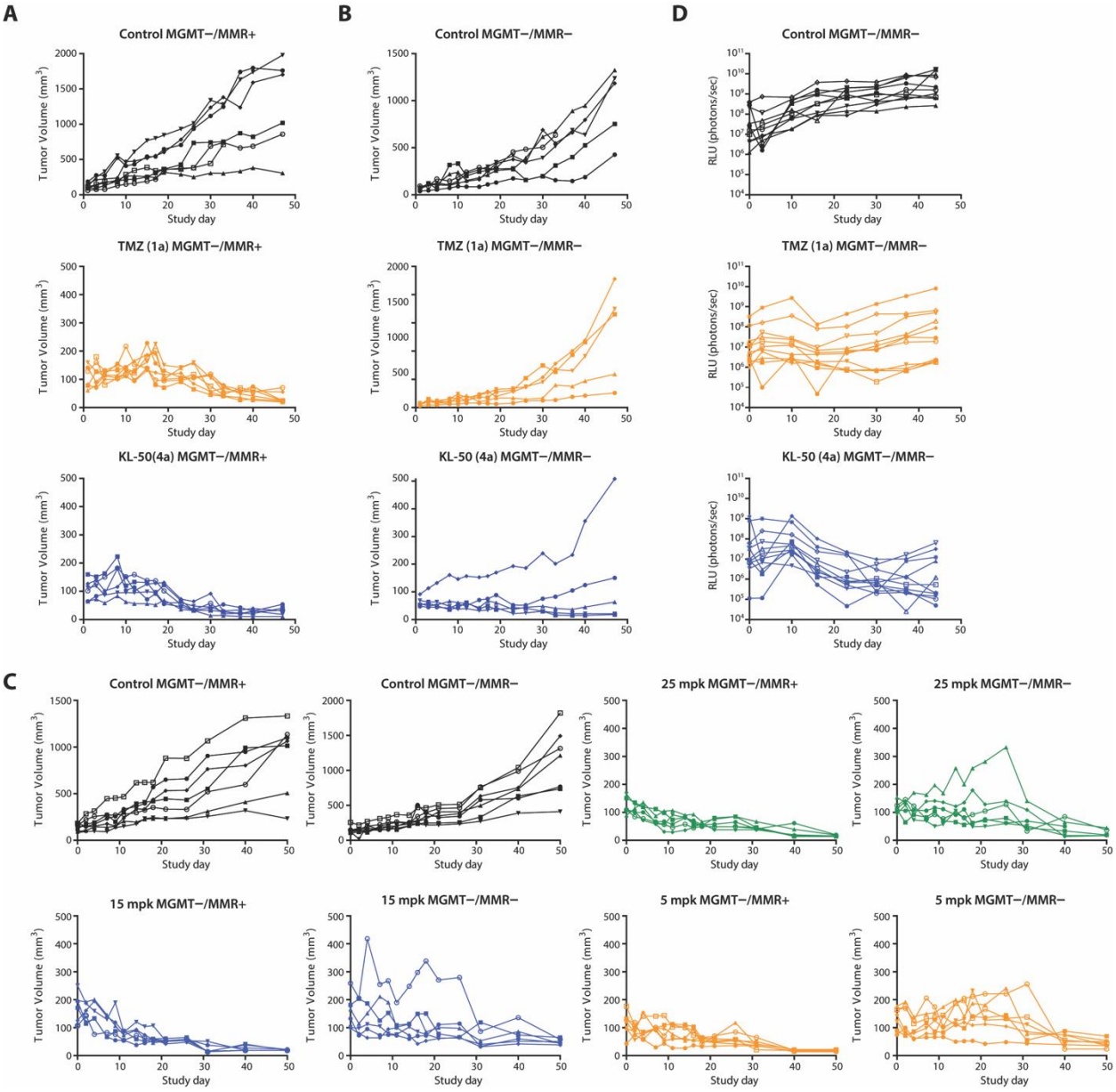

Fig. S10.

Spider plots tracking individual mouse tumor response to treatment. (**A**) Spider plots tracking LN229 MGMT–/MMR+ flank tumor volume of each mouse in response to treatment with P.O. 10% cyclodextrin vehicle control, TMZ (**1a**, 5 mg/kg MWF × 3 weeks), or KL-50 (**4a**, 5 mg/kg MWF × 3 weeks). (**B**) Spider plots tracking LN229 MGMT–/MMR– flank tumor volume of each mouse in response to treatment with PO 10% cyclodextrin vehicle control, TMZ (**1a**, 5 mg/kg MWF × 3 weeks), or KL-50 (**4a**, 5 mg/kg MWF × 3 weeks). (**C**) Spider plots tracking LN229 MGMT–/MMR+ and LN229 MGMT–/MMR– flank tumor volume in response to treatment with PO 10% cyclodextrin control, PO KL-50 (**4a**, 15 mg/kg MWF × 3 weeks), PO KL-50 (**4a**, 25 mg/kg M–F × 1 week), or IP KL-50 (**4a**, 5 mg/kg MWF × 3 weeks). (**D**) Spider plots tracking LN229 MGMT–/MMR– intracranial tumor size as measured by relative light units (photons/sec)

in response to PO treatment with 10% cyclodextrin vehicle control, TMZ (**1a,** 25 mg/kg M–F × 1 week), or KL-50 (**4a**, 25 mg/kg M–F × 1 week).

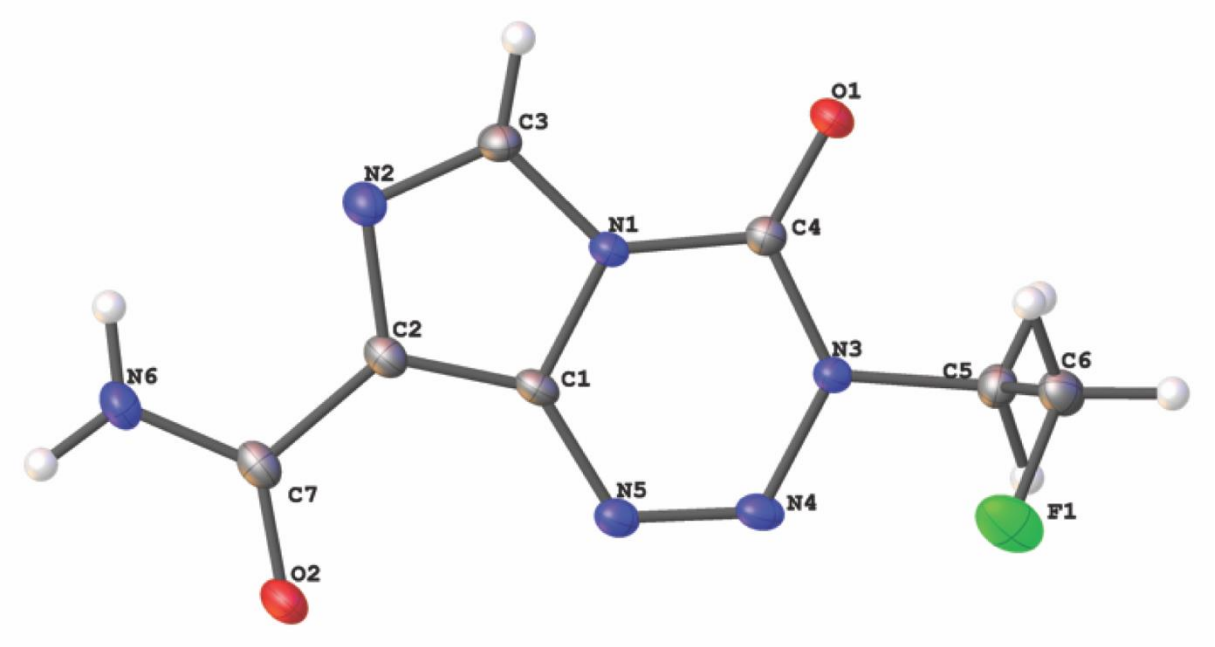

Fig. S11.

The complete numbering scheme for Polymorph I of KL-50 (4a). Shown with 50% thermal ellipsoid probability levels. The hydrogen atoms are shown as circles for clarity.

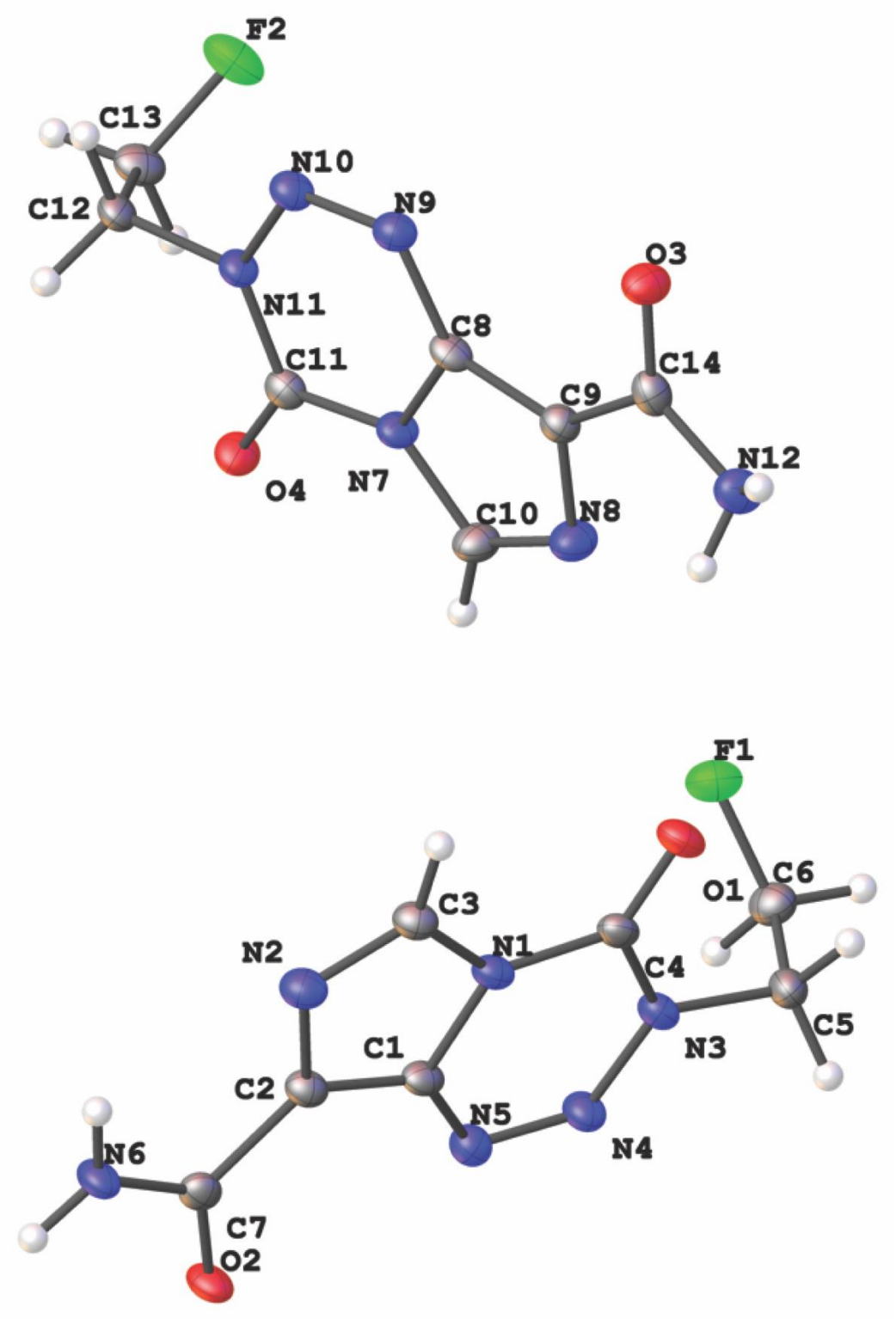

Fig. S12.

The complete numbering scheme for Polymorph II of KL-50 (4a). Shown with 50% thermal ellipsoid probability levels. The hydrogen atoms are shown as circles for clarity.

Synthetic Procedures

*Synthesis of KL-50 (**4a**)*

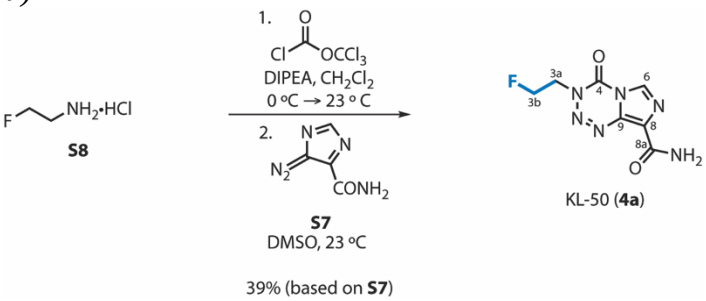

A mixture of fluoroethylamine hydrochloride (3.32 g, 33.3 mmol, 1 equiv), and *N*,*N*-di-*iso*-propyl ethylamine (12.2 mL, 70.0 mmol, 2.10 equiv) in dichloromethane (80 mL) was added dropwise via syringe pump over 45 min to a solution of diphosgene (2.40 mL, 20.0 mmol, 0.60 equiv) in dichloromethane (80 mL) at 0 °C (CAUTION: Gas evolution!). Upon completion of the addition, the cooling bath was removed, and the reaction mixture was allowed to warm to 23 °C over 15 min. The warmed product mixture was immediately transferred to a separatory funnel. The organic layer was washed sequentially with 1 N aqueous hydrochloric acid solution (100 mL, precooled to 0 °C) and saturated aqueous sodium chloride solution (100 mL, precooled to 0 °C). The washed organic layer was dried over magnesium sulfate. The dried solution was filtered, and the filtrate was concentrated (330 mTorr, 31 °C). The unpurified isocyanate so obtained was used directly in the following step.

The unpurified isocyanate obtained in the preceding step (nominally 16.7 mmol, 1.75 equiv) was added dropwise via syringe to a solution of the diazonium **S7** (1.31 g, 9.54 mmol, 1 equiv) in dimethyl sulfoxide (10 mL) at 23 °C. Upon completion of the addition, the reaction vessel was covered with aluminum foil. The reaction mixture was stirred for 16 h at 23 °C. The product mixture was concentrated under a stream of nitrogen. The residue obtained was suspended in dichloromethane and purified by automated flash-column chromatography (eluting with 100% dichloromethane initially, grading to 5% methanol–dichloromethane, linear gradient) to provide KL-50 (**4a**) as a white crystalline powder (840 mg, 39% based on the diazonium **S7**).

^{1}H NMR (400 MHz, DMSO-d_6) δ 8.85 (s, 1H, H_6), 7.83 (s, 1H, NH), 7.70 (s, 1H, NH), 4.82 (dt, J = 47.0, 4.9 Hz, 2H, H_{3b}), 4.62 (dt, J = 26.0, 4.7 Hz, 2H, H_{3a}). ^{13}C NMR (151 MHz, DMSO-d_6) δ 161.5 (C_{8a}), 139.2 (C_4), 134.2 (C_9), 131.0 (C_8), 128.9 (C_6), 80.8 (d, J = 168.7 Hz, C_{3b}), 49.1 (d, J = 20.8 Hz, C_{3a}). ^{19}F NMR (376 MHz, DMSO-d_6) δ –222.66 (tt, J = 47.0, 26.1 Hz). IR (ATR-FTIR), cm^{-1}: 3459 (w), 3119 (m), 1736 (s), 1675 (s). HRMS-ESI (*m/z*): $[M + H]^+$ calcd for $[C_7H_8FN_6O_2]^+$ 227.0688, found 227.0676.

*Synthesis of the imidazolyl triazene **10***

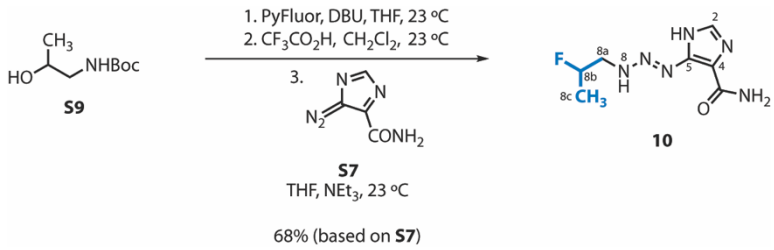

Tert-butyl (2-hydroxypropyl)carbamate (1.72 mL, 10.0 mmol, 1 equiv) was added dropwise via syringe to a mixture of PyFluor (1.77 g, 11.0 mmol, 1.10 equiv) in tetrahydrofuran (10 mL) at 23°C. 1,8-Diazabicyclo(5.4.0)undec-7-ene (3.00 mL, 20.0 mmol, 2.00 equiv) was immediately added dropwise and the reaction mixture was stirred for 48 h at 23 °C under ambient atmosphere. The product mixture was diluted with water (15 mL) and the resulting biphasic mixture was transferred to a separatory funnel. The layers that formed were separated and the aqueous layer was extracted with ethyl acetate (2 × 15 mL). The organic layers were combined and the combined organic layer was washed sequentially with 1 N aqueous hydrochloric acid solution (2 × 25 mL) and saturated aqueous sodium chloride solution (2 × 25 mL). The washed organic layer was dried over sodium sulfate. The dried solution was then filtered and the filtrate concentrated to provide *tert*-butyl (2-fluoropropyl)carbamate as a clear colorless oil.

The unpurified product obtained in the preceding step (nominally 6 mmol, 1 equiv) was added to a mixture of dichloromethane (30 mL) and trifluoroacetic acid (10 mL) at 23°C. The reaction mixture was stirred for 12 h at 23 °C under ambient atmosphere. The product mixture was concentrated to provide 2-fluoropropylamine trifluoroacetic acid as an opaque oil with excess equivalents of trifluoroacetic acid. The unpurified product obtained in this way (nominally 6 mmol) was dissolved in tetrahydrofuran (10 mL) to generate a working nominal 0.6 M solution for future reactions.

A solution of 2-fluoropropylamine trifluoroacetic acid in tetrahydrofuran (4.40 mL, 2.64 mmol, 1.05 equiv) and triethylamine (1.40 mL, 10 mmol, 4.00 equiv) were added sequentially dropwise via syringe to a suspension of the diazonium **S7** (343 mg, 2.50 mmol, 1 equiv) in tetrahydrofuran (15 mL) at 23°C. The reaction mixture was stirred for 6 h at 23 °C. The precipitate that formed was collected by vacuum filtration. The precipitate was washed sequentially with ethyl acetate (2 × 15 mL) and diethyl ether (2 × 15 mL). The washed precipitate was dried in vacuo to afford the imidazolyl triazene **10** as a light tan powder (365 mg, 68%, based on the diazonium **S7**).

^{1}H NMR (600 MHz, DMSO-d_6) δ 12.65 (s, 1H, NH), 10.92 (s, 1H, H_8), 7.54 (s, 1H, H_2), 7.45 (br s, 1H, NH), 7.21 (s, 1H, NH), 4.98 (br d, J = 49 Hz, 1H, H_{8b}), 3.87 – 3.55 (m, 2H, H_{8a}), 1.34 (dd, J = 23.9, 6.3 Hz, 3H, H_{8c}). ^{13}C NMR (151 MHz, DMSO-d_6) δ 161.0 ($C_{quat.}$), 149.5 – 148.9 (br, $C_{quat.}$)*, 135.6 (C_2), 115.9 ($C_{quat.}$), 87.1 (d, J = 166.6 Hz, C_{8b}), 48.1 (d, J = 22.3 Hz, C_{8a}), 18.8 (d, J = 21.7 Hz, C_{8c}). ^{19}F NMR (376 MHz, DMSO-d_6) δ –174.43 (dq, J = 47.7, 23.9 Hz). IR (ATR-FTIR), cm^{-1}: 3480 (w), 3249 (m), 3077 (m), 1638 (s), 1590 (s), 1427 (s), 1397 (s). HRMS-ESI (*m/z*): $[M + H]^+$ calcd for $[C_7H_{12}FN_6O]^+$ 215.1052, found 215.1048.

*Broad peak tentatively attributed to a quaternary carbon from the imidazolyl triazene **10**.

*Synthesis of imidazolyl triazene **11***

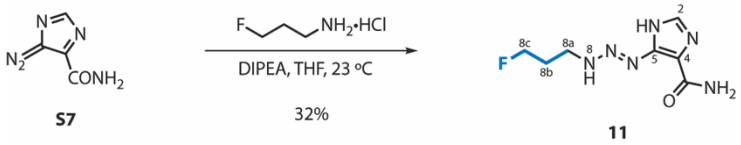

N,*N*-Di-*iso*-propyl ethylamine (834 µL, 4.55 mmol, 1.25 equiv) was added dropwise via syringe to a mixture of (3-fluoropropyl)amine hydrochloride (410 mg, 3.65 mmol, 1 equiv) and the diazonium **S7** (500 mg, 3.65 mmol, 1 equiv) in tetrahydrofuran (25 mL) at 23 ºC. The reaction mixture was stirred for 6 h at 23 °C. The precipitate that formed was collected by vacuum filtration. The precipitate was washed sequentially with ethyl acetate (2 × 15 mL) and ether (2 × 15 mL). The washed precipitate was dried in vacuo to afford the imidazolyl triazene **11** as a light tan powder (251 mg, 32%).

^{1}H NMR (400 MHz, DMSO-d_6) δ 12.63 (s, 1H, NH), 10.72 (s, 1H, H_8), 7.54 (s, 1H, H_2), 7.46 (s, 1H, NH), 7.28 (s, 1H, NH), 4.54 (dt, J = 47.3, 5.9 Hz, 2H, H_{8c}), 3.60 – 3.50 (m, 2H, H_{8a}), 2.09 – 1.94 (m, 2H, H_{8b}). ^{13}C NMR (151 MHz, DMSO-d_6) δ 135.6 (C_2), 81.6 (C_{8c}), 39.3 (C_{8a}), 26.4 (C_{8b}).* ^{19}F NMR (376 MHz, DMSO-d_6) δ –219.23 (tt, J = 47.1, 26.1 Hz). IR (ATR-FTIR), cm^{-1}: 3483 (w), 3269 (m), 3082 (m), 1640 (m), 1587 (m), 1392 (m). HRMS-ESI (*m/z*): $[M + Na]^+$ calcd for $[C_7H_{11}FN_6NaO]^+$ 237.0871, found 237.0986.

*Due to peak broadening, we obtained ^{13}C shifts from an ^{1}H-^{13}C HSQC spectrum; as such, quaternary carbons are not reported. We hypothesize that the peak broadening is caused by chemical exchange.

Crystallographic Analysis of KL-50 (4a)

Procedure for Crystal Growth

Single crystals of KL-50 (**4a**) suitable for X-ray analysis were obtained by vapor diffusion of dry benzene (3 mL, precipitating solvent) into a syringe filtered (Millipore Sigma, 0.22 µm, hydrophilic polyvinylidene fluoride, 33 mm, gamma sterilized, catalogue number SLGV033RS) solution of KL-50 (**4a**) (3.6 mg) in dry dichloromethane (3 mL, solubilizing solvent) at 23 ºC. This yielded two polymorphs of KL-50 (**4a**) designated Polymorph I ($P2_1/n$ space group, CCDC number 2122008) and Polymorph II (Cc space group, CCDC number 2122009).

Experimental Procedure for Polymorph I of KL-50 (**4a**)

Low-temperature diffraction data (ω-scans) were collected on a Rigaku MicroMax-007HF diffractometer coupled to a Dectris Pilatus3R detector with Mo Kα (λ = 0.71073 Å) for the structure of 007c-21083. The diffraction images were processed and scaled using Rigaku Oxford Diffraction software (CrysAlisPro; Rigaku OD: The Woodlands, TX, 2015). The structure was solved with SHELXT and was refined against F^2 on all data by full-matrix least squares with SHELXL (Sheldrick, G. M. Acta Cryst. 2008, A64, 112–122). All non-hydrogen atoms were refined anisotropically. Hydrogen atoms were included in the model at geometrically calculated positions and refined using a riding model. The isotropic displacement parameters of all hydrogen atoms were fixed to 1.2 times the U value of the atoms to which they are linked (1.5 times for methyl groups). The full numbering scheme of compound 007c-21083 can be found in the full details of the X-ray structure determination (CIF), which is included as Supporting Information. CCDC number 2122008 (007c-21083) contains the supplementary crystallographic data for this paper. These data can be obtained free of charge from The Cambridge Crystallographic Data Center via www.ccdc.cam.ac.uk/data_request/cif.

Crystal data and structure refinement for Polymorph I of KL-50 (**4a**)

Identification code	007c-21083	
Empirical formula	C7 H7 F N6 O2	
Formula weight	226.19	
Temperature	93(2) K	
Wavelength	0.71073 Å	
Crystal system	Monoclinic	
Space group	$P2_1/n$	
Unit cell dimensions	a = 7.1861(5) Å	α = 90°.
	b = 7.6918(5) Å	β = 96.758(6)°.
	c = 16.4546(12) Å	γ = 90°.
Volume	903.19(11) $Å^3$	
Z	4	
Density (calculated)	1.663 Mg/m^3	
Absorption coefficient	0.141 mm^{-1}	
F(000)	464	
Crystal size	0.200 x 0.200 x 0.020 mm^3	
Crystal color and habit	Colorless Plate	
Diffractometer	Dectris Pilatus 3R	
Theta range for data collection	2.927 to 31.467°.	
Index ranges	-9<=h<=10, -10<=k<=9, -23<=l<=19	
Reflections collected	9836	
Independent reflections	2539 [R(int) = 0.0300]	
Observed reflections (I > 2sigma(I))	2135	
Completeness to theta = 25.242°	99.9 %	
Absorption correction	Semi-empirical from equivalents	
Max. and min. transmission	1.00000 and 0.31047	
Solution method	SHELXT-2014/5 (Sheldrick, 2014)	
Refinement method	SHELXL-2014/7 (Sheldrick, 2014)	
Data / restraints / parameters	2539 / 0 / 145	
Goodness-of-fit on F^2	1.050	
Final R indices [I>2sigma(I)]	R1 = 0.0358, wR2 = 0.0885	
R indices (all data)	R1 = 0.0450, wR2 = 0.0929	
Largest diff. peak and hole	0.360 and -0.250 $e.Å^{-3}$	

Experimental procedure for Polymorph II of KL-50 (**4a**)

Low-temperature diffraction data (ω-scans) were collected on a Rigaku MicroMax-007HF diffractometer coupled to a Saturn994+ CCD detector with Cu Kα (λ = 1.54178 Å) for the structure of 007b-21124. The diffraction images were processed and scaled using Rigaku Oxford Diffraction software (CrysAlisPro; Rigaku OD: The Woodlands, TX, 2015). The structure was solved with SHELXT and was refined against F^2 on all data by full-matrix least squares with SHELXL (Sheldrick, G. M. Acta Cryst. 2008, A64, 112–122). All non-hydrogen atoms were refined anisotropically. Hydrogen atoms were included in the model at geometrically calculated positions and refined using a riding model. The isotropic displacement parameters of all hydrogen atoms were fixed to 1.2 times the U value of the atoms to which they are linked (1.5 times for methyl groups). The full numbering scheme of compound 007b-21124 can be found in the full details of the X-ray structure determination (CIF), which is included as Supporting Information. CCDC number 2122009 (007b-21124) contains the supplementary crystallographic data for this paper. These data can be obtained free of charge from The Cambridge Crystallographic Data Center via www.ccdc.cam.ac.uk/data_request/cif

Crystal data and structure refinement for Polymorph II of KL-50 (**4a**)

Identification code	007b-21124	
Empirical formula	C7 H7 F N6 O2	
Formula weight	226.19	
Temperature	93(2) K	
Wavelength	1.54184 Å	
Crystal system	Monoclinic	
Space group	Cc	
Unit cell dimensions	a = 6.6061(2) Å	α = 90°.
	b = 23.1652(6) Å	β = 95.987(2)°.
	c = 11.9879(3) Å	γ = 90°.
Volume	1824.52(9) $Å^3$	
Z	8	
Density (calculated)	1.647 Mg/m^3	
Absorption coefficient	1.218 mm^{-1}	
F(000)	928	
Crystal size	0.200 x 0.020 x 0.020 mm^3	
Crystal color and habit	Colorless Needle	
Diffractometer	Rigaku Saturn 944+ CCD	
Theta range for data collection	3.816 to 66.573°.	
Index ranges	-7<=h<=7, -27<=k<=27, -14<=l<=14	
Reflections collected	31349	
Independent reflections	3204 [R(int) = 0.0818]	
Observed reflections (I > 2sigma(I))	2950	
Completeness to theta = 66.573°	100.0 %	
Absorption correction	Semi-empirical from equivalents	
Max. and min. transmission	1.00000 and 0.59718	
Solution method	SHELXT-2014/5 (Sheldrick, 2014)	
Refinement method	SHELXL-2014/7 (Sheldrick, 2014)	
Data / restraints / parameters	3204 / 2 / 291	
Goodness-of-fit on F^2	1.041	
Final R indices [I>2sigma(I)]	R1 = 0.0330, wR2 = 0.0770	
R indices (all data)	R1 = 0.0381, wR2 = 0.0795	
Absolute structure parameter	0.1(2)	
Extinction coefficient	n/a	
Largest diff. peak and hole	0.225 and -0.223 e.$Å^{-3}$	

Catalogue of Nuclear Magnetic Resonance Spectra

^{1}H NMR, 400 MHz, DMSO-d_6

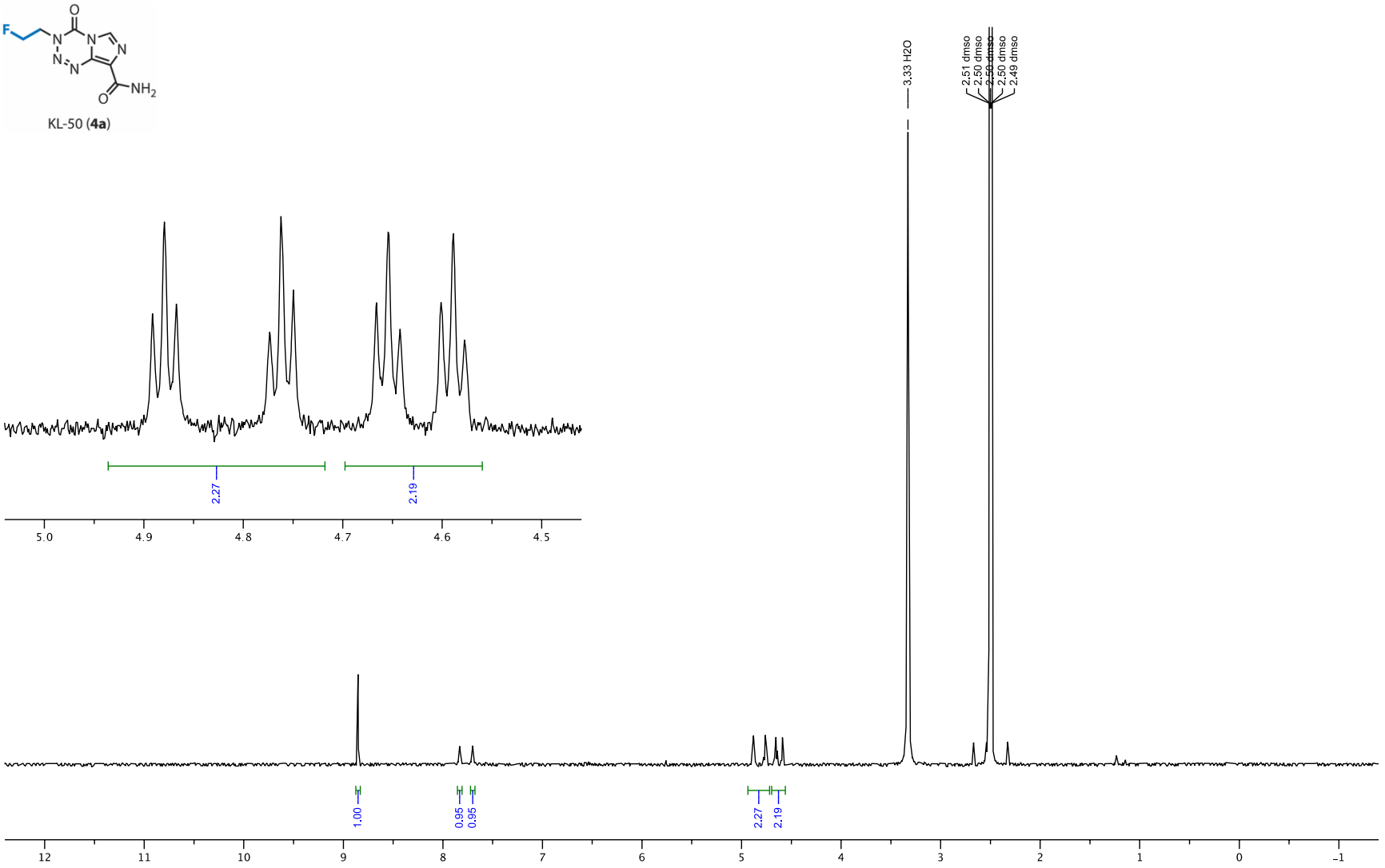

^{13}C NMR, 151 MHz, DMSO-d_6

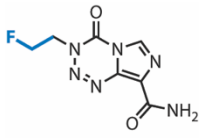

KL-50 (**4a**)

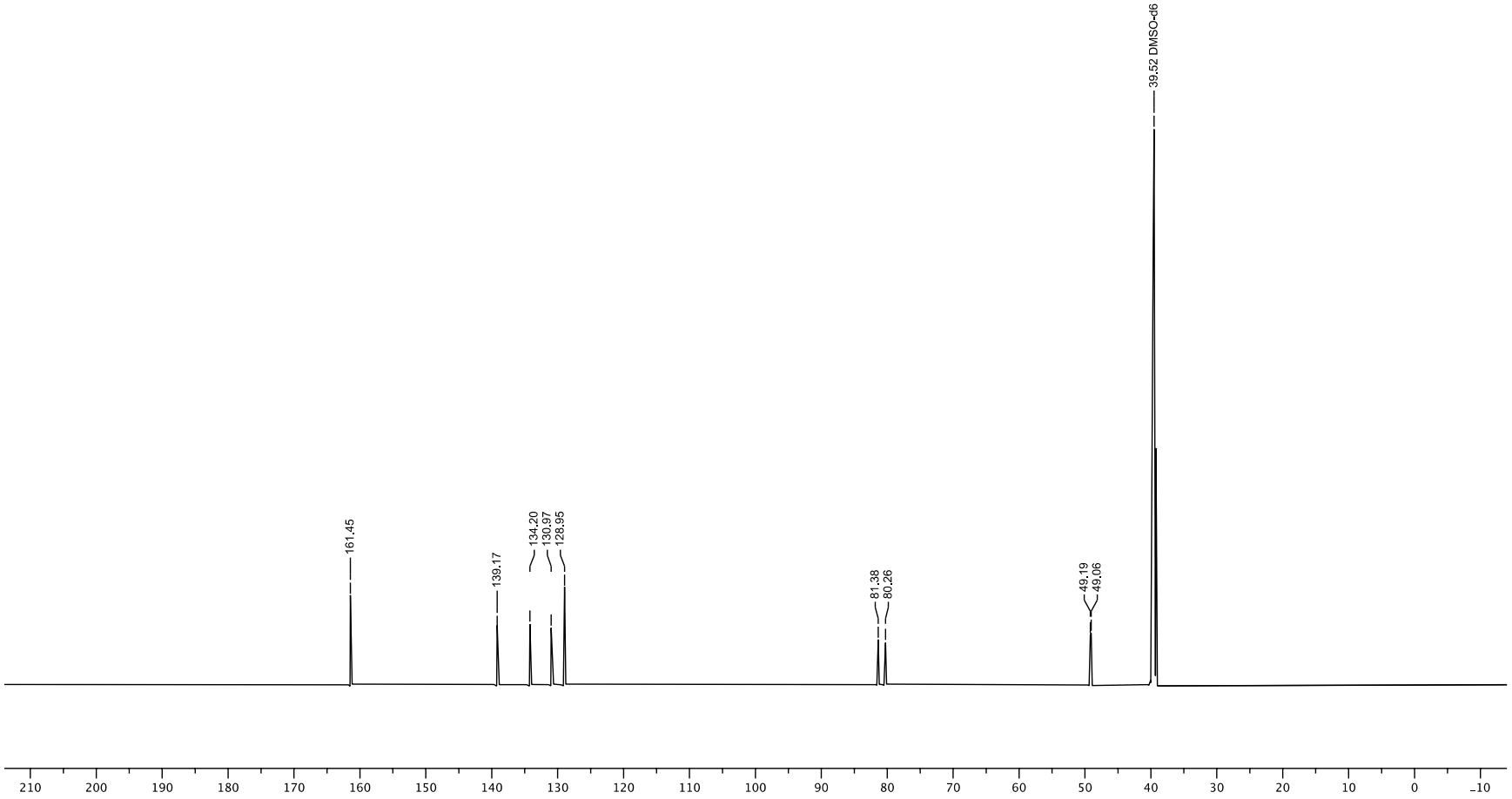

^{19}F NMR, 376 MHz, DMSO-d_6

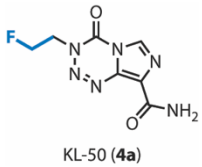

KL-50 (**4a**)

^{1}H-^{13}C HSQC NMR, 600 MHz, DMSO-d_6 | Notes: (1) Blue = CH/CH$_3$; Red = CH$_2$. (2) Data acquired with $^{1}J_{CH}$ = 146 Hz.

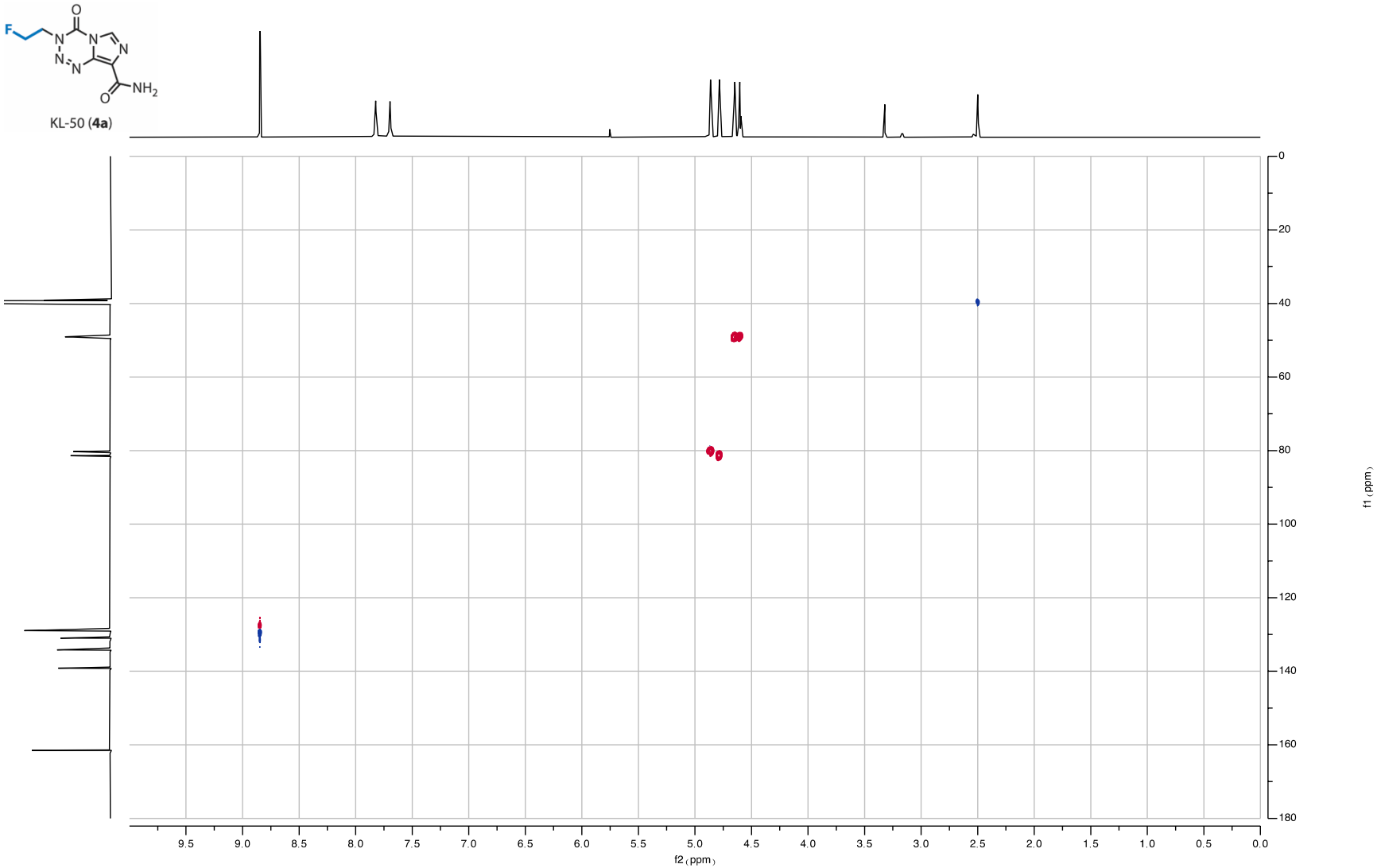

^{1}H-^{13}C HSQC NMR, 600 MHz, DMSO-d_6 | Notes: (1) Blue = CH/CH_3; Red = CH_2. (2) Data acquired with $^{1}J_{CH}$ = 225 Hz.

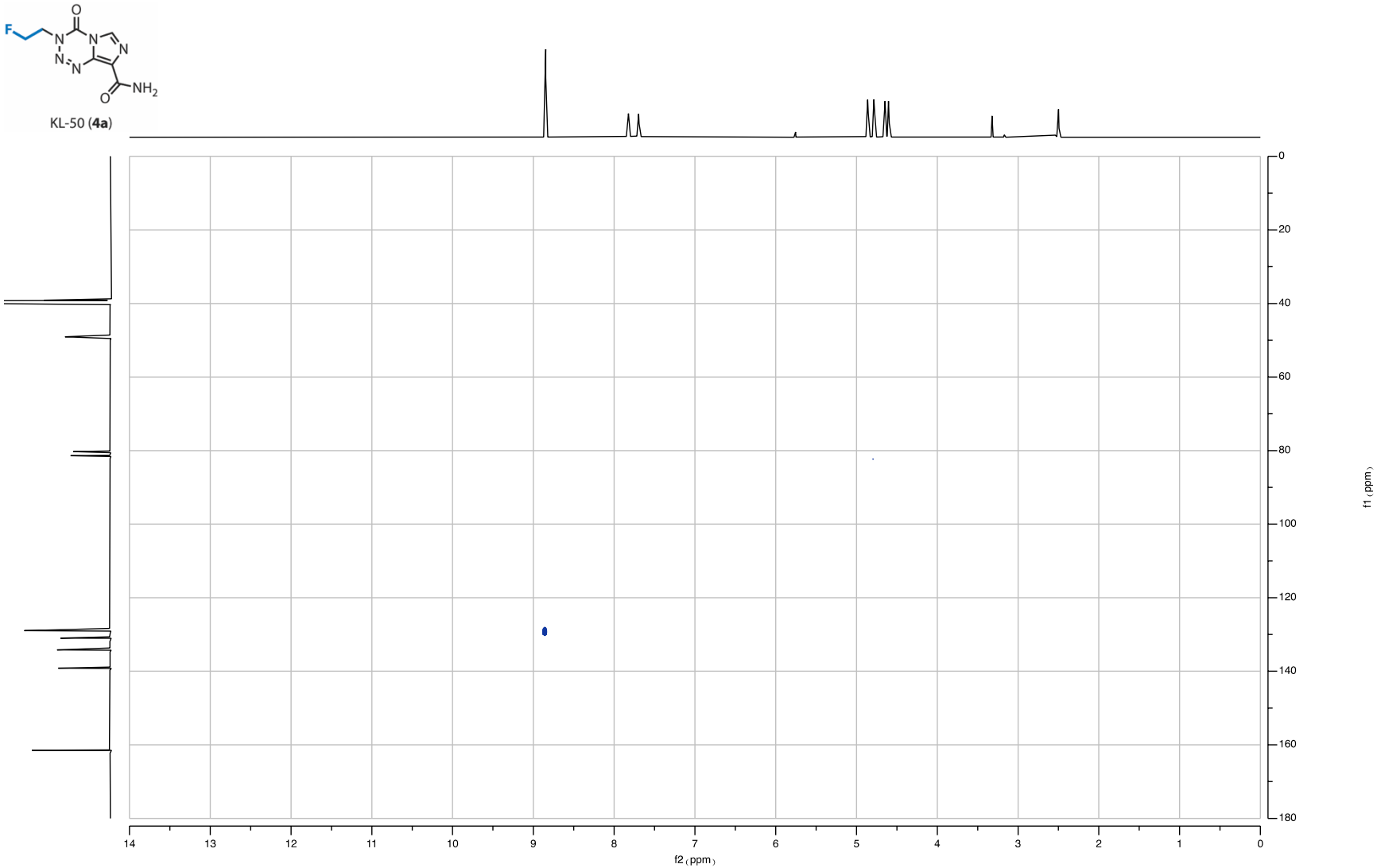

^{1}H-^{1}H gCOSY NMR, 600 MHz, DMSO-d_6

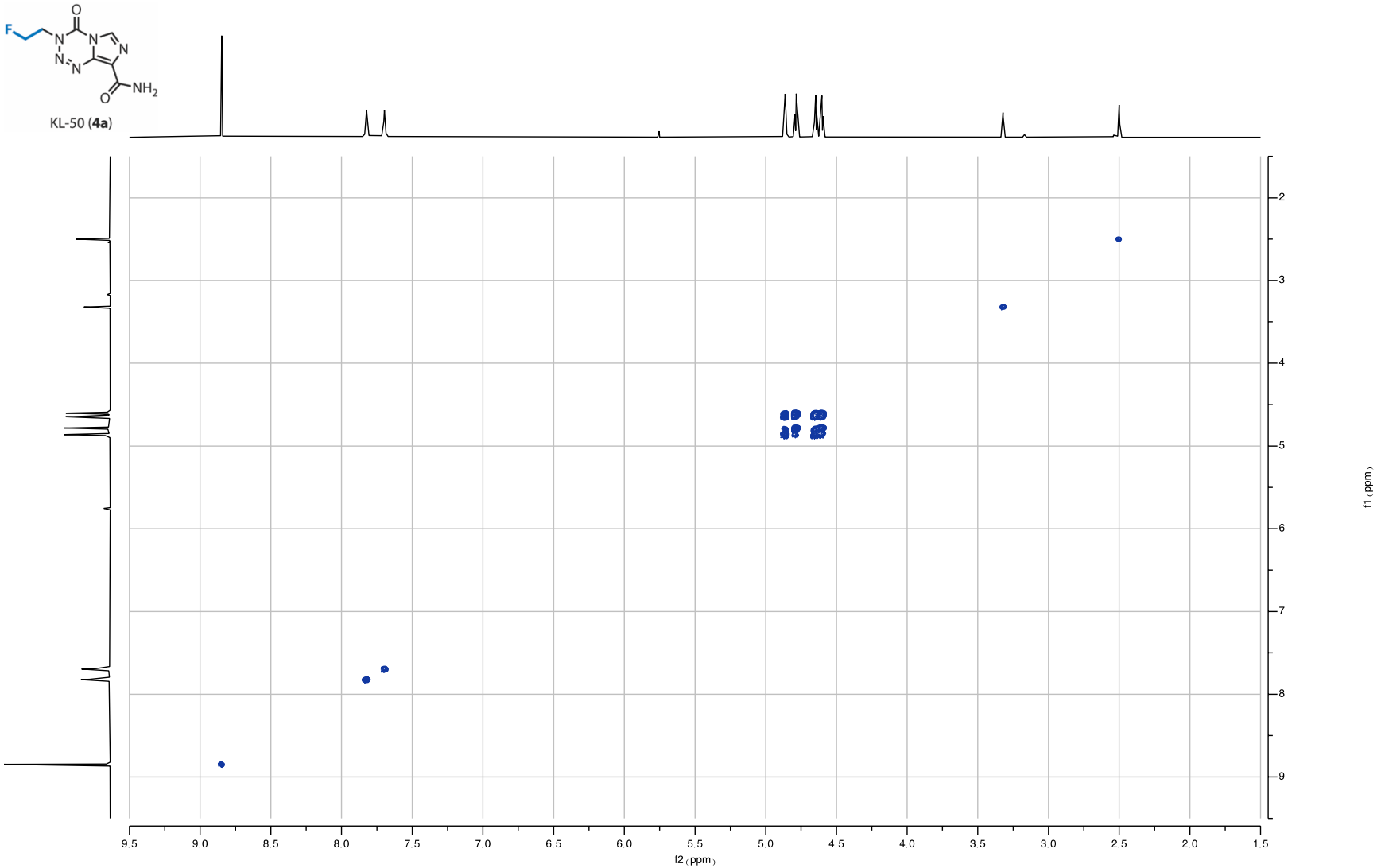

^{1}H-^{13}C gHMBC NMR, 600 MHz, DMSO-d_6

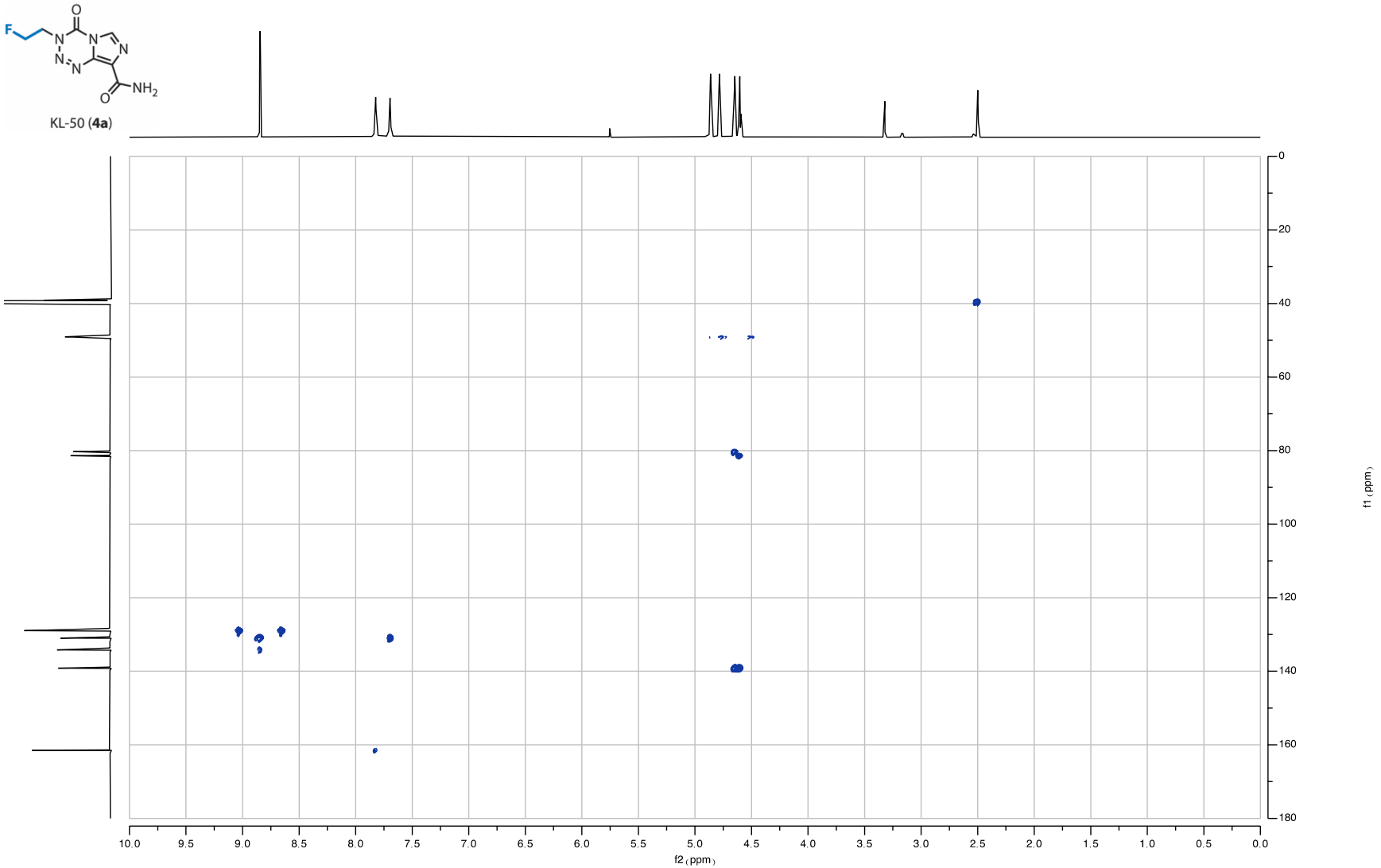

^{1}H NMR, 600 MHz, DMSO-d_6

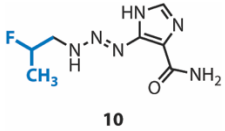

10

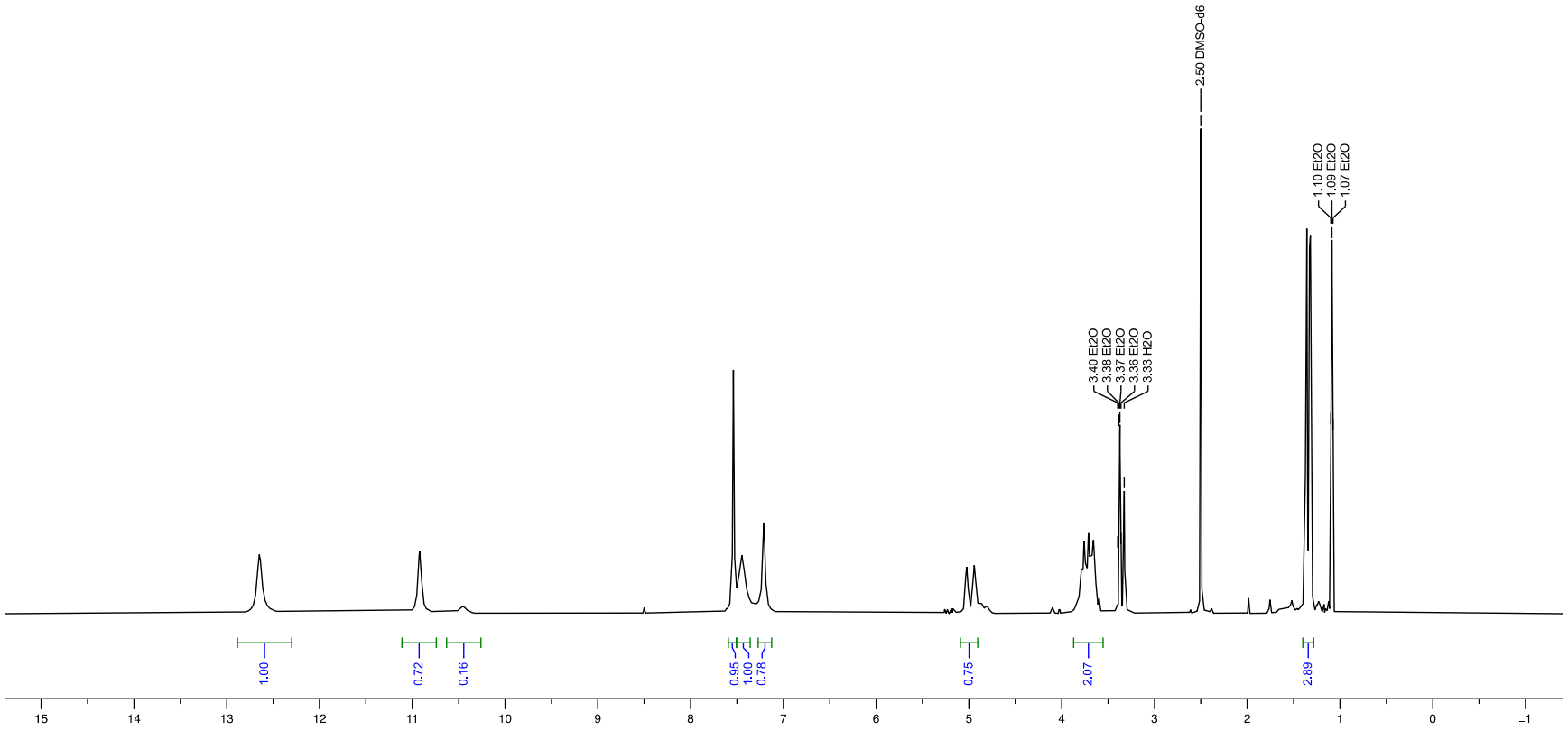

^{13}C NMR, 151 MHz, DMSO-d_6

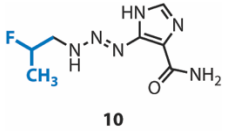

10

^{19}F NMR, 376 MHz, DMSO-d_6

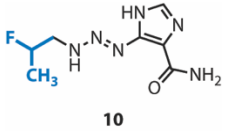

10

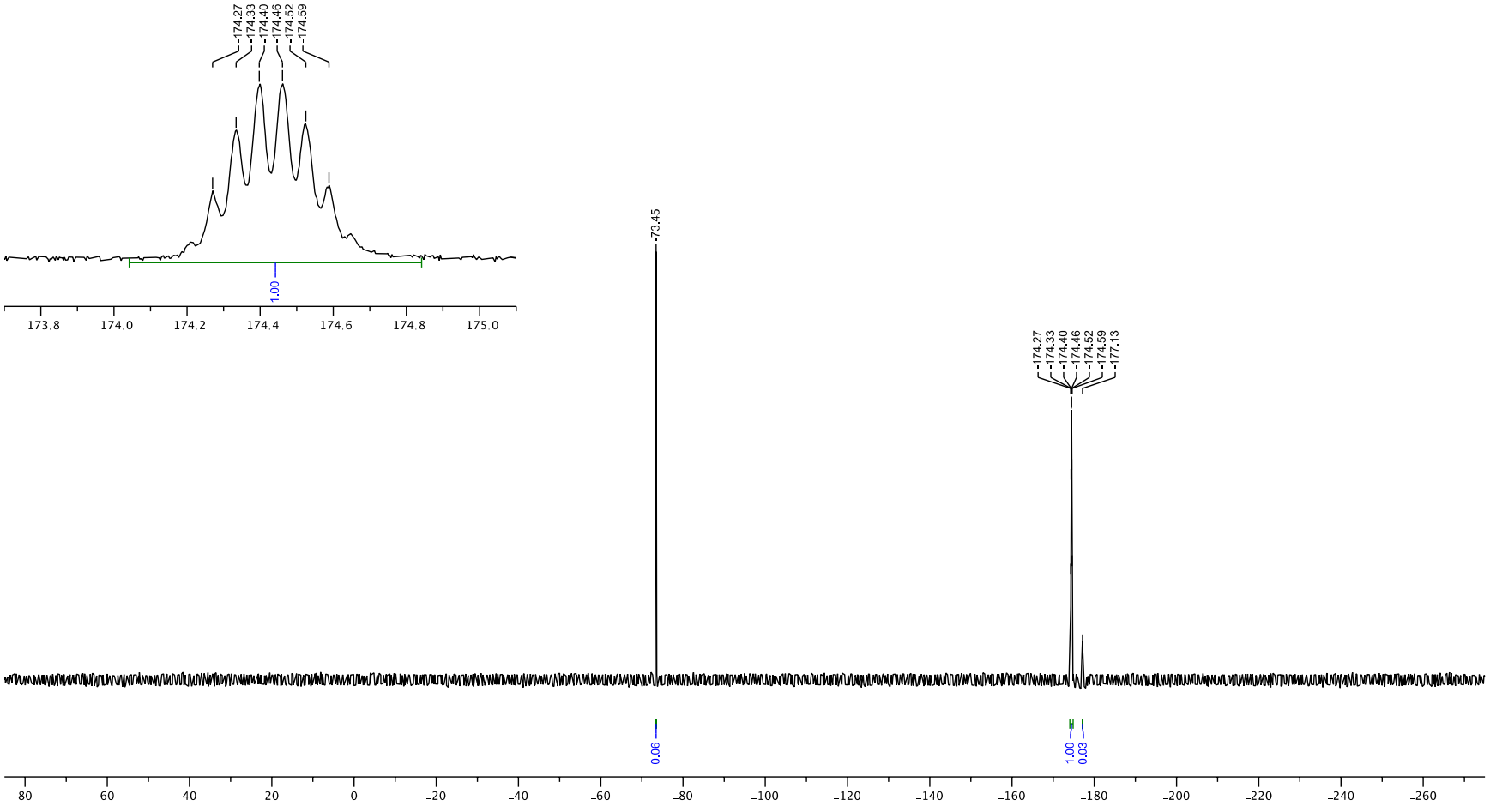

^{1}H-^{13}C HSQC NMR, 600 MHz, DMSO-d_6 | Note: Blue = CH/CH_3; Red = CH_2.

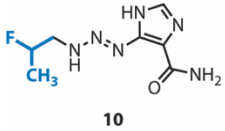

10

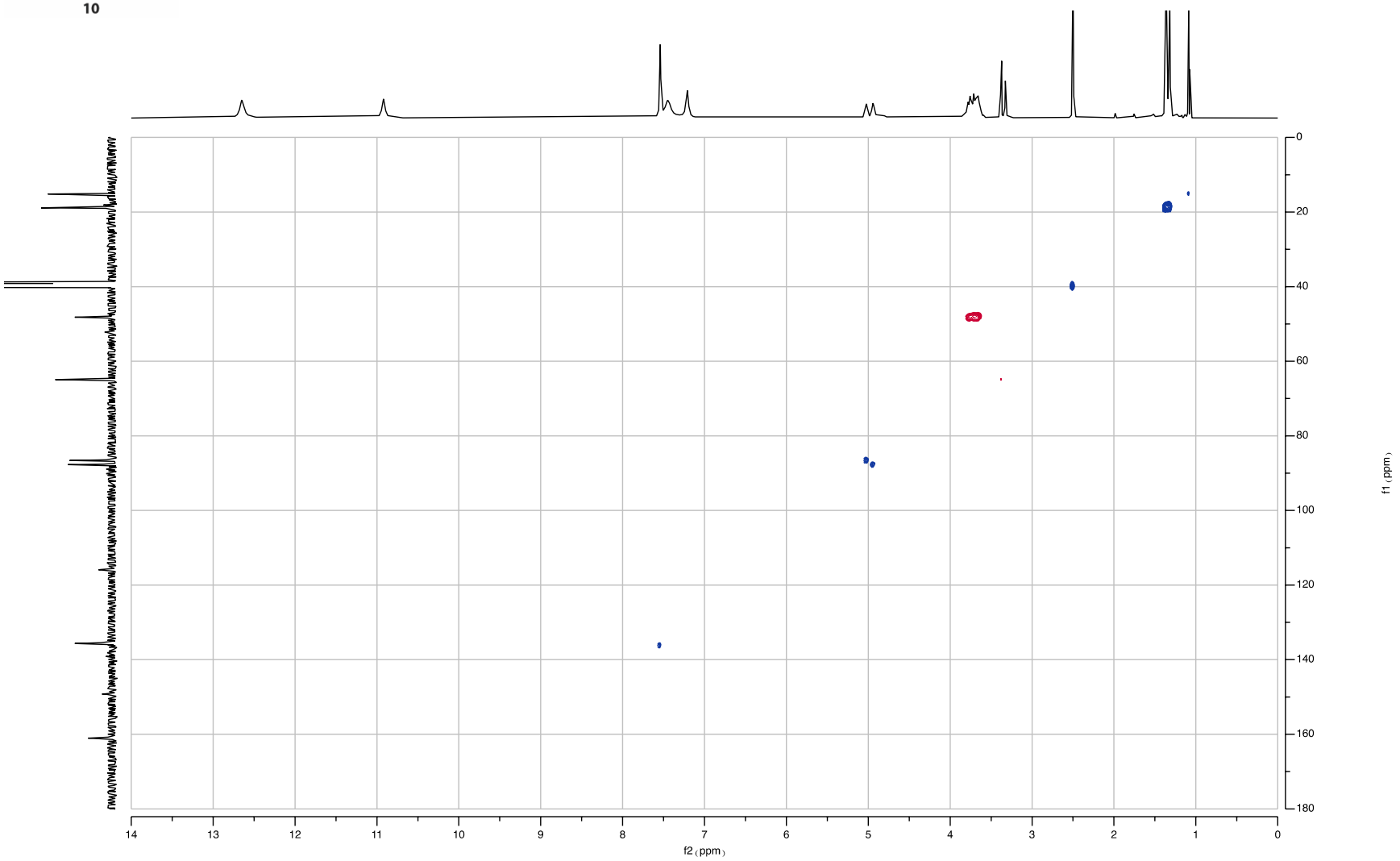

^{1}H-^{1}H gCOSY NMR, 600 MHz, DMSO-d_6

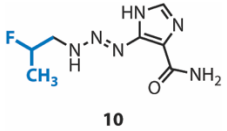

10

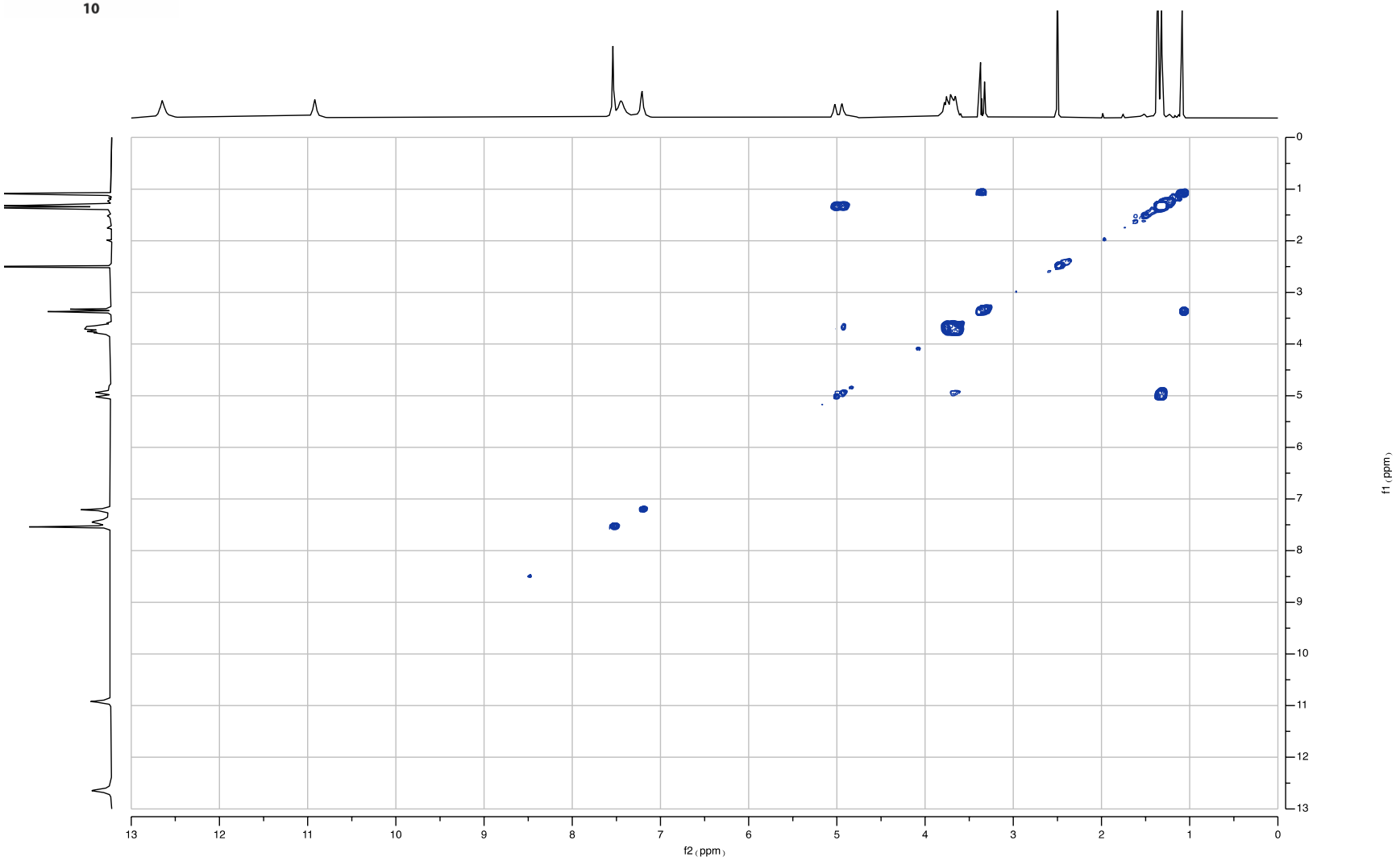

^{1}H NMR, 400 MHz, DMSO-d_6

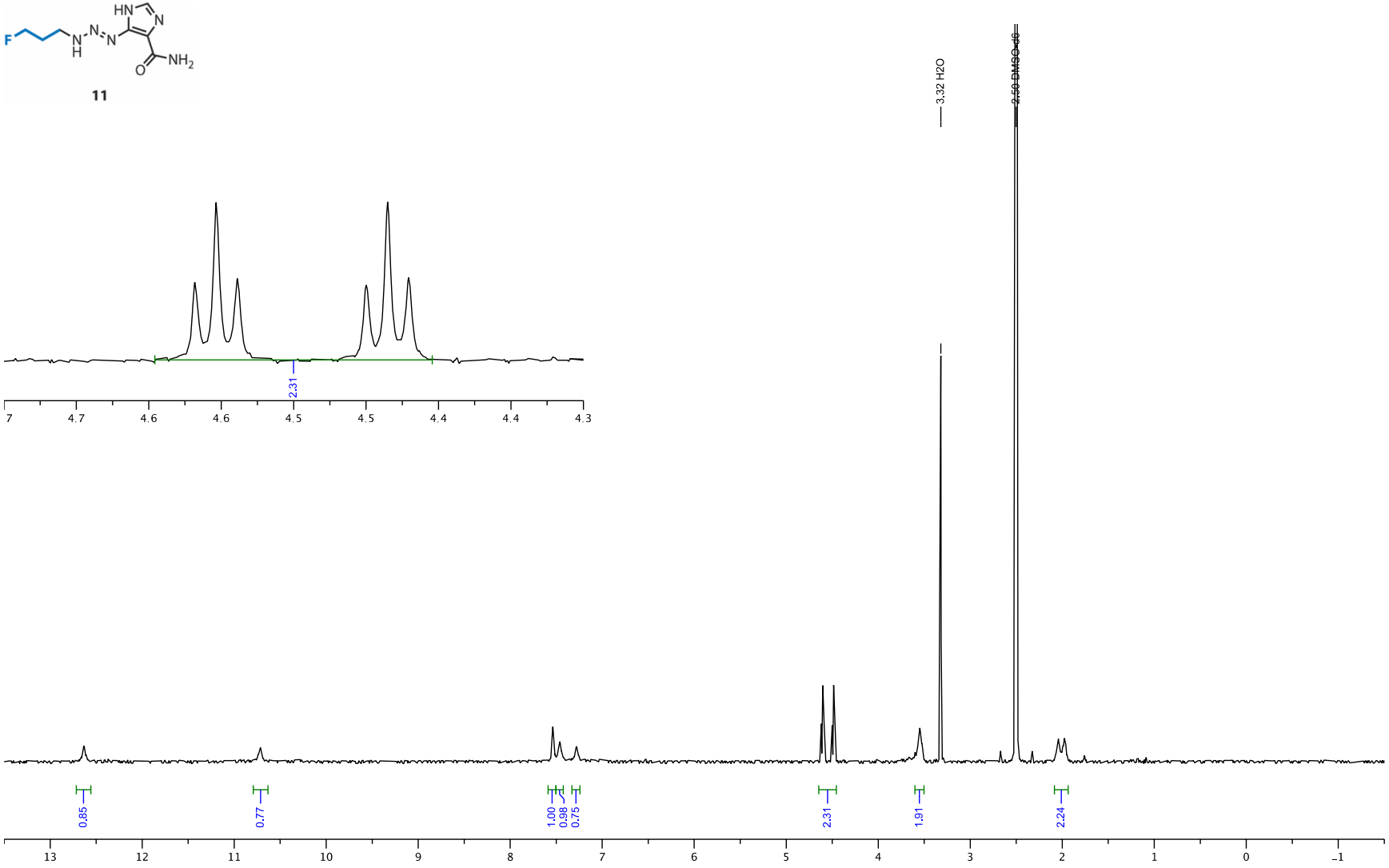

^{19}F NMR, 376 MHz, DMSO-d_6

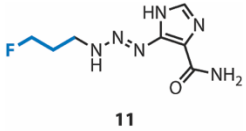

11

^{1}H-^{13}C HSQC NMR, 600 MHz, DMSO-d_6 | Note: Blue = CH/CH_3; Red = CH_2.

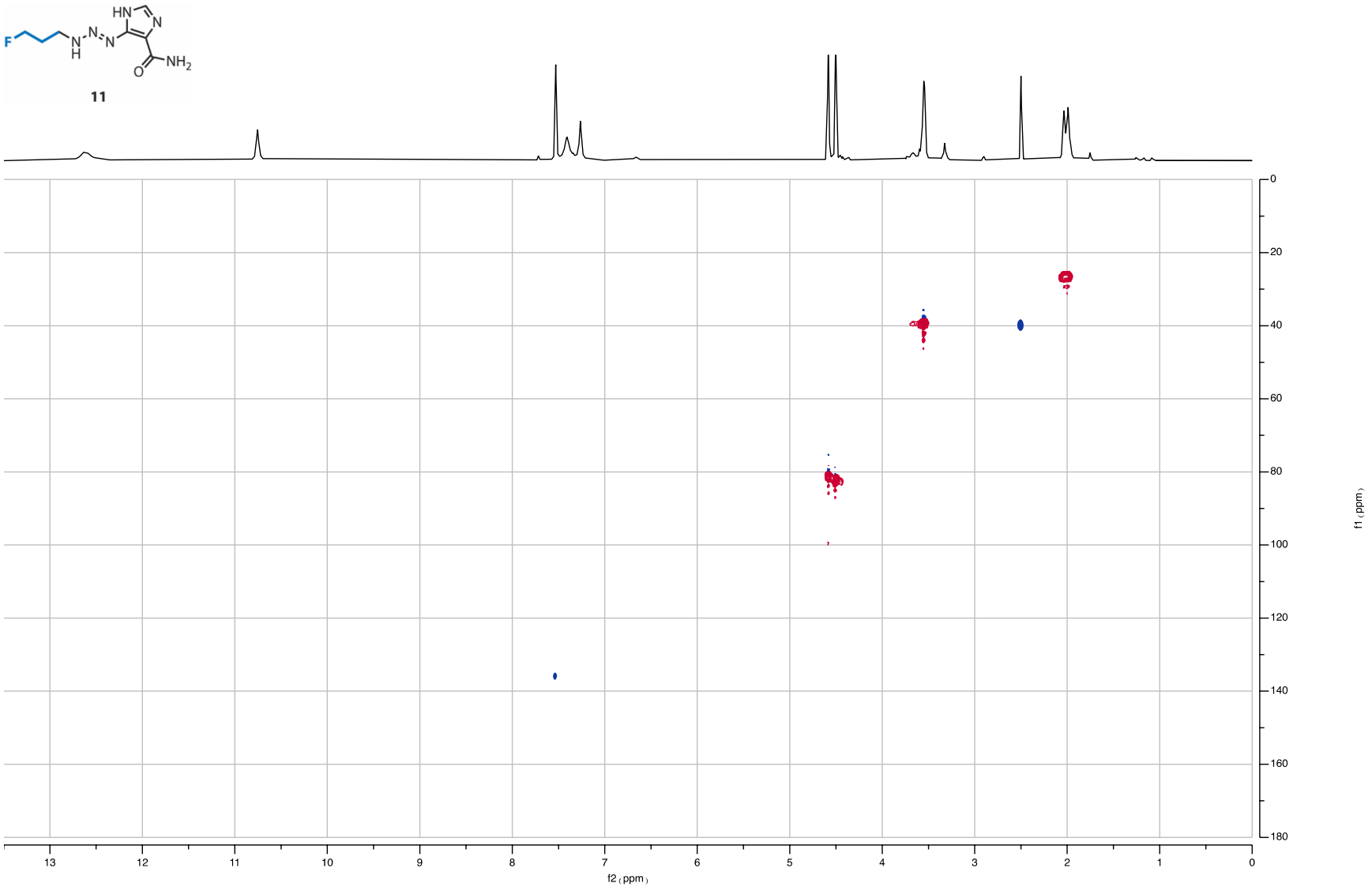

^{1}H-^{1}H COSY NMR, 600 MHz, DMSO-d_6

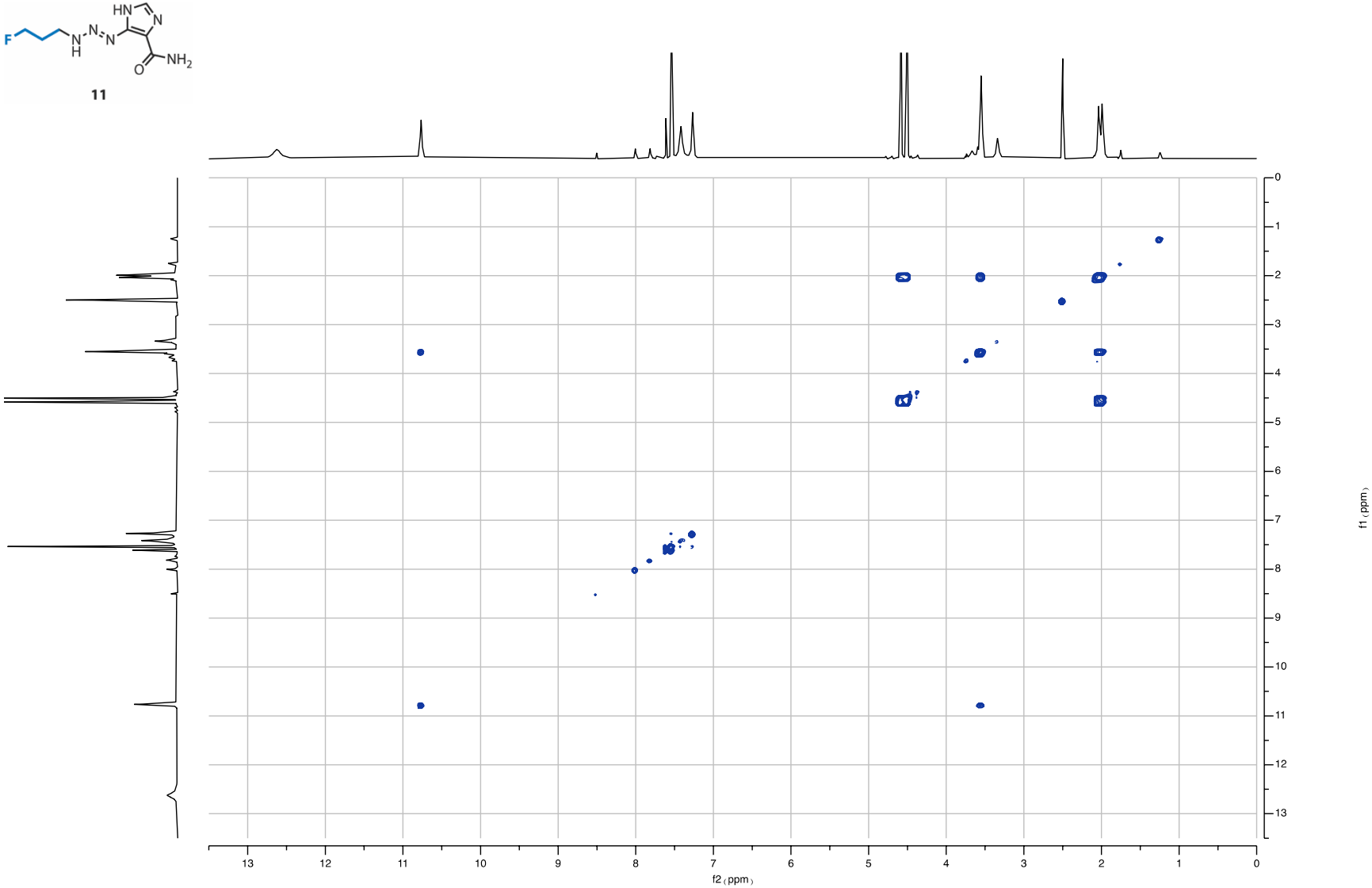

References and Notes

1. N. J. Curtin, DNA repair dysregulation from cancer driver to therapeutic target. *Nat. Rev. Cancer* **12**, 801–817 (2012).

2. H. E. Bryant, N. Schultz, H. D. Thomas, K. M. Parker, D. Flower, E. Lopez, S. Kyle, M. Meuth, N. J. Curtin, T. Helleday, Specific killing of BRCA2-deficient tumours with inhibitors of poly(ADP-ribose) polymerase. *Nature* **434**, 913–917 (2005).

3. H. Farmer, N. McCabe, C. J. Lord, A. N. J. Tutt, D. A. Johnson, T. B. Richardson, M. Santarosa, K. J. Dillon, I. Hickson, C. Knights, N. M. B. Martin, S. P. Jackson, G. C. M. Smith, A. Ashworth, Targeting the DNA repair defect in BRCA mutant cells as a therapeutic strategy. *Nature* **434**, 917–921 (2005).

4. D. Zatreanu, H. M. R. Robinson, O. Alkhatib, M. Boursier, H. Finch, L. Geo, D. Grande, V. Grinkevich, R. A. Heald, S. Langdon, J. Majithiya, C. McWhirter, N. M. B. Martin, S. Moore, J. Neves, E. Rajendra, M. Ranzani, T. Schaedler, M. Stockley, K. Wiggins, R. Brough, S. Sridhar, A. Gulati, N. Shao, L. M. Badder, D. Novo, E. G. Knight, R. Marlow, S. Haider, E. Callen, G. Hewitt, J. Schimmel, R. Prevo, C. Alli, A. Ferdinand, C. Bell, P. Blencowe, C. Bot, M. Calder, M. Charles, J. Curry, T. Ekwuru, K. Ewings, W. Krajewski, E. MacDonald, H. McCarron, L. Pang, C. Pedder, L. Rigoreau, M. Swarbrick, E. Wheatley, S. Willis, A. C. Wong, A. Nussenzweig, M. Tijsterman, A. Tutt, S. J. Boulton, G. S. Higgins, S. J. Pettitt, G. C. M. Smith, C. J. Lord, Polθ inhibitors elicit BRCA-gene synthetic lethality and target PARP inhibitor resistance. *Nat. Commun.* **12**, 3636 (2021).

5. P. M. Reaper, M. R. Griffiths, J. M. Long, J.-D. Charrier, S. Maccormick, P. A. Charlton, J. M. C. Golec, J. R. Pollard, Selective killing of ATM- or p53-deficient cancer cells through inhibition of ATR. *Nat. Chem. Biol.* **7**, 428–430 (2011).

6. S. Lieb, S. Blaha-Ostermann, E. Kamper, J. Rippka, C. Schwarz, K. Ehrenhöfer-Wölfer, A. Schlattl, A. Wernitznig, J. J. Lipp, K. Nagasaka, P. van der Lelij, G. Bader, M. Koi, A. Goel, R. A. Neumüller, J.-M. Peters, N. Kraut, M. A. Pearson, M. Petronczki, S. Wöhrle, Werner syndrome helicase is a selective vulnerability of microsatellite instability-high tumor cells. *eLife* **8**, e43333 (2019).

7. J. Murai, S. Y. Huang, B. B. Das, A. Renaud, Y. Zhang, J. H. Doroshow, J. Ji, S. Takeda, Y. Pommier, Trapping of PARP1 and PARP2 by clinical PARP inhibitors. *Cancer Res.* **72**, 5588–5599 (2012).

8. M. P. Dias, S. C. Moser, S. Ganesan, J. Jonkers, Understanding and overcoming resistance to PARP inhibitors in cancer therapy. *Nat. Rev. Clin. Oncol.* **18**, 773–791 (2021).

9. M. A. Sabatino, M. Marabese, M. Ganzinelli, E. Caiola, C. Geroni, M. Broggini, Down-regulation of the nucleotide excision repair gene XPG as a new mechanism of drug resistance in human and murine cancer cells. *Mol. Cancer* **9**, 259 (2010).

10. N. Adachi, S. So, H. Koyama, Loss of nonhomologous end joining confers camptothecin resistance in DT40 cells. Implications for the repair of topoisomerase I-mediated DNA damage. *J. Biol. Chem.* **279**, 37343–37348 (2004).

11. S. E. Fordham, E. C. Matheson, K. Scott, J. A. E. Irving, J. M. Allan, DNA mismatch repair status affects cellular response to Ara-C and other anti-leukemic nucleoside analogs. *Leukemia* **25**, 1046–1049 (2011).

12. A. Sawant, A. Kothandapani, A. Zhitkovich, R. W. Sobol, S. M. Patrick, Role of mismatch repair proteins in the processing of cisplatin interstrand cross-links. *DNA Repair* **35**, 126–136 (2015).

13. E. H. Bell, P. Zhang, B. J. Fisher, D. R. Macdonald, J. P. McElroy, G. J. Lesser, J. Fleming, A. R. Chakraborty, Z. Liu, A. P. Becker, D. Fabian, K. D. Aldape, L. S. Ashby, M. Werner-Wasik, E. M. Walker, J.-P. Bahary, Y. Kwok, H. M. Yu, N. N. Laack, C. J. Schultz, H. J. Gray, H. I. Robins, M. P. Mehta, A. Chakravarti, Association of *MGMT* promoter methylation status with survival outcomes in patients with high-risk glioma treated with radiotherapy and temozolomide: An analysis from the NRG oncology/RTOG 0424 trial. *JAMA Oncol.* **4**, 1405–1409 (2018).

14. G.-M. Li, Mechanisms and functions of DNA mismatch repair. *Cell Res.* **18**, 85–98 (2008).

15. M. E. Hegi, A.-C. Diserens, T. Gorlia, M.-F. Hamou, N. de Tribolet, M. Weller, J. M. Kros, J. A. Hainfellner, W. Mason, L. Mariani, J. E. C. Bromberg, P. Hau, R. O. Mirimanoff, J. G. Cairncross, R. C. Janzer, R. Stupp, *MGMT* gene silencing and benefit from temozolomide in glioblastoma. *N. Engl. J. Med.* **352**, 997–1003 (2005).

16. K. Yoshimoto, M. Mizoguchi, N. Hata, H. Murata, R. Hatae, T. Amano, A. Nakamizo, T. Sasaki, Complex DNA repair pathways as possible therapeutic targets to overcome temozolomide resistance in glioblastoma. *Front. Oncol.* **2**, 186 (2012).

17. M. Touat, Y. Y. Li, A. N. Boynton, L. F. Spurr, J. B. Iorgulescu, C. L. Bohrson, I. Cortes-Ciriano, C. Birzu, J. E. Geduldig, K. Pelton, M. J. Lim-Fat, S. Pal, R. Ferrer-Luna, S. H. Ramkissoon, F. Dubois, C. Bellamy, N. Currimjee, J. Bonardi, K. Qian, P. Ho, S. Malinowski, L. Taquet, R. E. Jones, A. Shetty, K.-H. Chow, R. Sharaf, D. Pavlick, L. A. Albacker, N. Younan, C. Baldini, M. Verreault, M. Giry, E. Guillerm, S. Ammari, F. Beuvon, K. Mokhtari, A. Alentorn, C. Dehais, C. Houillier, F. Laigle-Donadey, D. Psimaras, E. Q. Lee, L. Nayak, J. R. McFaline-Figueroa, A. Carpentier, P. Cornu, L. Capelle, B. Mathon, J. S. Barnholtz-Sloan, A. Chakravarti, W. L. Bi, E. A. Chiocca, K. P. Fehnel, S. Alexandrescu, S. N. Chi, D. Haas-Kogan, T. T. Batchelor, G. M. Frampton, B. M. Alexander, R. Y. Huang, A. H. Ligon, F. Coulet, J.-Y. Delattre, K. Hoang-Xuan, D. M. Meredith, S. Santagata, A. Duval, M. Sanson, A. D. Cherniack, P. Y. Wen, D. A. Reardon, A. Marabelle, P. J. Park, A. Idbaih, R. Beroukhim, P. Bandopadhayay, F. Bielle, K. L. Ligon, Mechanisms and therapeutic implications of hypermutation in gliomas. *Nature* **580**, 517–523 (2020).

18. Y. Yu, J. Villanueva-Meyer, M. R. Grimmer, S. Hilz, D. A. Solomon, S. Choi, M. Wahl, T. Mazor, C. Hong, A. Shai, J. J. Phillips, B. H. Wainer, M. McDermott, D. Haas-Kogan, J. W. Taylor, N. Butowski, J. L. Clarke, M. S. Berger, A. M. Molinaro, S. M. Chang, J. F. Costello, N. A. Oberheim Bush, Temozolomide-induced hypermutation is associated with distant recurrence and reduced survival after high-grade transformation of low-grade *IDH*-mutant gliomas. *Neuro-oncol.* **23**, 1872–1884 (2021).

19. W. P. Tong, M. C. Kirk, D. B. Ludlum, Mechanism of action of the nitrosoureas—V. Formation of O^6-(2-fluoroethyl)guanine and its probable role in the crosslinking of deoxyribonucleic acid. *Biochem. Pharmacol.* **32**, 2011–2015 (1983).

20. S. Hentschel, J. Alzeer, T. Angelov, O. D. Schärer, N. W. Luedtke, Synthesis of DNA interstrand cross-links using a photocaged nucleobase. *Angew. Chem. Int. Ed.* **51**, 3466–3469 (2012).

21. C. L. Chan, Z. Wu, T. Ciardelli, A. Eastman, E. Bresnick, Kinetic and DNA-binding properties of recombinant human O^6-methylguanine-DNA methyltransferase. *Arch. Biochem. Biophys.* **300**, 193–200 (1993).

22. T. Shibata, N. Glynn, T. B. McMurry, R. S. McElhinney, G. P. Margison, D. M. Williams, Novel synthesis of O^6-alkylguanine containing oligodeoxyribonucleotides as substrates for the human DNA repair protein, O^6-methylguanine DNA methyltransferase (MGMT). *Nucleic Acids Res.* **34**, 1884–1891 (2006).

23. A. E. Pegg, Multifaceted roles of alkyltransferase and related proteins in DNA repair, DNA damage, resistance to chemotherapy, and research tools. *Chem. Res. Toxicol.* **24**, 618–639 (2011).

24. H. Martinez, A. Rebeyrol, T. B. Nelms, W. R. Dolbier Jr., Impact of fluorine substituents on the rates of nucleophilic aliphatic substitution and β-elimination. *J. Fluor. Chem.* **135**, 167–175 (2012).

25. Y. Wang, R. T. Wheelhouse, L. Zhao, D. A. F. Langnel, M. F. G. Stevens, Antitumour imidazotetrazines. Part 36.1 Conversion of 5-aminoimidazole-4-carboxamide to imidazo[5,1-d][1,2,3,5]tetrazin-4(3H)-ones and imidazo[1,5-a][1,3,5]triazin-4(3H)-ones related in structure to the antitumour agents temozolomide and mitozolomide. *J. Chem. Soc., Perkin Trans. 1* **10**, 1669–1676 (1998).

26. J. A. Double, M. C. Bibby, Therapeutic index: A vital component in selection of anticancer agents for clinical trial. *J. Natl. Cancer Inst.* **81**, 988–994 (1989).

27. L. J. Fairbairn, N. Chinnasamy, L. S. Lashford, D. Chinnasamy, J. A. Rafferty, Enhancing hemopoietic drug resistance: A rationale for reconsidering the clinical use of mitozolomide. *Cancer Gene Ther.* **7**, 233–239 (2000).

28. L. Liu, S. Markowitz, S. L. Gerson, Mismatch repair mutations override alkyltransferase in conferring resistance to temozolomide but not to 1,3-bis(2-chloroethyl)nitrosourea. *Cancer Res.* **56**, 5375–5379 (1996).

29. J. Jiricny, Postreplicative mismatch repair. *Cold Spring Harb. Perspect. Biol.* **5**, a012633 (2013).

30. S. Ganesa, A. Sule, R. K. Sundaram, R. S. Bindra, Mismatch repair proteins play a role in ATR activation upon temozolomide treatment in MGMT-methylated glioblastoma. *Sci. Rep.* **12**, 5827 (2022).

31. D. J. McKenna, M. Gallus, S. R. McKeown, C. S. Downes, V. J. McKelvey-Martin, Modification of the alkaline Comet assay to allow simultaneous evaluation of mitomycin C-induced DNA cross-link damage and repair of specific DNA sequences in RT4 cells. *DNA Repair* **2**, 879–890 (2003).

32. T. P. Brent, P. E. Gonzaga, D. G. Smith, in *DNA Repair Mechanisms and Their Biological Implications in Mammalian Cells*, M. W. Lambert, J. Laval, Eds. (Springer, 1989), pp. 619–638.

33. N. Bossuet-Greif, J. Vignard, F. Taieb, G. Mirey, D. Dubois, C. Petit, E. Oswald, J.-P. Nougayrède, The colibactin genotoxin generates DNA interstrand cross-links in infected cells. *mBio* **9**, e02393-17 (2018).

34. M. Xue, K. M. Wernke, S. B. Herzon, Depurination of colibactin-derived interstrand cross-links. *Biochemistry* **59**, 892–900 (2020).

35. C. B. Jackson, S. I. Noorbakhsh, R. K. Sundaram, A. N. Kalathil, S. Ganesa, L. Jia, H. Breslin, D. M. Burgenske, O. Gilad, J. N. Sarkaria, R. S. Bindra, Temozolomide sensitizes MGMT-deficient tumor cells to ATR inhibitors. *Cancer Res.* **79**, 4331–4338 (2019).

36. K. Rothkamm, S. Barnard, J. Moquet, M. Ellender, Z. Rana, S. Burdak-Rothkamm, DNA damage foci: Meaning and significance. *Environ. Mol. Mutagen.* **56**, 491–504 (2015).

37. V. O'Brien, R. Brown, Signalling cell cycle arrest and cell death through the MMR System. *Carcinogenesis* **27**, 682–692 (2006).

38. D. Vare, P. Groth, R. Carlsson, F. Johansson, K. Erixon, D. Jenssen, DNA interstrand crosslinks induce a potent replication block followed by formation and repair of double strand breaks in intact mammalian cells. *DNA Repair* **11**, 976–985 (2012).

39. Y. Matsuno, Y. Atsumi, A. Shimizu, K. Katayama, H. Fujimori, M. Hyodo, Y. Minakawa, Y. Nakatsu, S. Kaneko, R. Hamamoto, T. Shimamura, S. Miyano, T. Tsuzuki, F. Hanaoka, K. I. Yoshioka, Replication stress triggers microsatellite destabilization and hypermutation leading to clonal expansion in vitro. *Nat. Commun.* **10**, 3925 (2019).

40. C. C. Chen, T. Taniguchi, A. D'Andrea, The Fanconi anemia (FA) pathway confers glioma resistance to DNA alkylating agents. *J. Mol. Med.* **85**, 497–509 (2007).

41. N. Mojas, M. Lopes, J. Jiricny, Mismatch repair-dependent processing of methylation damage gives rise to persistent single-stranded gaps in newly replicated DNA. *Genes Dev.* **21**, 3342–3355 (2007).

42. N. Leelatian, C. S. Hong, R. S. Bindra, The role of mismatch repair in glioblastoma multiforme treatment response and resistance. *Neurosurg. Clin. N. Am.* **32**, 171–180 (2021).

43. Y. Pan, The dark side of fluorine. *ACS Med. Chem. Lett.* **10**, 1016–1019 (2019).

44. S. Parker, M. C. Kirk, D. B. Ludlum, Synthesis and characterization of O^6-(2-chloroethyl)guanine: A putative intermediate in the cytotoxic reaction of chloroethylnitrosoureas with DNA. *Biochem. Biophys. Res. Commun.* **148**, 1124–1128 (1987).

45. D. B. Ludlum, W. P. Tong, Mechanism of action of the nitrosoureas—II. Formation of fluoroethylguanosine from the reaction of bis-fluoroethyl nitrosourea and guanosine. *Biochem. Pharmacol.* **27**, 2391–2394 (1978).

46. K. Morimoto, M. E. Dolan, D. Scicchitano, A. E. Pegg, Repair of O^6-propylguanine and O^6-butylguanine in DNA by O^6-alkylguanine-DNA alkyltransferases from rat liver and *E. coli*. *Carcinogenesis* **6**, 1027–1031 (1985).

47. P. D. Lawley, D. H. Phillips, DNA adducts from chemotherapeutic agents. *Mutation Res.* **355**, 13–40 (1996).

48. B. Stratenwerth, S. M. Geisen, Y. He, L. Beltzig, S. J. Sturla, B. Kaina, Molecular dosimetry of temozolomide: Quantification of critical lesions, correlation to cell death responses, and threshold doses. *Mol. Cancer Ther.* **20**, 1789–1799 (2021).

49. M. Esteller, S. R. Hamilton, P. C. Burger, S. B. Baylin, J. G. Herman, Inactivation of the DNA repair gene O^6-methylguanine-DNA methyltransferase by promoter hypermethylation is a common event in primary human neoplasia. *Cancer Res.* **59**, 793–797 (1999).

50. A. Thomas, M. Tanaka, J. Trepel, W. C. Reinhold, V. N. Rajapakse, Y. Pommier, Temozolomide in the era of precision medicine. *Cancer Res.* **77**, 823–826 (2017).

51. H. Davies, D. Glodzik, S. Morganella, L. R. Yates, J. Staaf, X. Zou, M. Ramakrishna, S. Martin, S. Boyault, A. M. Sieuwerts, P. T. Simpson, T. A. King, K. Raine, J. E. Eyfjord, G. Kong, Å. Borg, E. Birney, H. G. Stunnenberg, M. J. van de Vijver, A.-L. Børresen-Dale, J. W. M. Martens, P. N. Span, S. R. Lakhani, A. Vincent-Salomon, C. Sotiriou, A. Tutt, A. M. Thompson, S. Van Laere, A. L. Richardson, A. Viari, P. J. Campbell, M. R. Stratton, S. Nik-Zainal, HRDetect is a predictor of BRCA1 and BRCA2 deficiency based on mutational signatures. *Nat. Med.* **23**, 517–525 (2017).

52. D. P. Cahill, P. J. Codd, T. T. Batchelor, W. T. Curry, D. N. Louis, MSH6 inactivation and emergent temozolomide resistance in human glioblastomas. *Clin. Neurosurg.* **55**, 165–171 (2008).

53. R. L. Svec, L. Furiassi, C. G. Skibinski, T. M. Fan, G. J. Riggins, P. J. Hergenrother, Tunable stability of imidazotetrazines leads to a potent compound for glioblastoma. *ACS Chem. Biol.* **13**, 3206–3216 (2018).

54. W. C. Still, M. Kahn, A. Mitra, Rapid chromatographic technique for preparative separations with moderate resolution. *J. Org. Chem.* **43**, 2923–2925 (1978).

55. A. B. Pangborn, M. A. Giardello, R. H. Grubbs, R. K. Rosen, F. J. Timmers, Safe and convenient procedure for solvent purification. *Organometallics* **15**, 1518–1520 (1996).

56. C. K. Moseley, S. M. Carlin, R. Neelamegam, J. M. Hooker, An efficient and practical radiosynthesis of [^{11}C]temozolomide. *Org. Lett.* **14**, 5872–5875 (2012).

57. G. U. Baig, M. F. G. Stevens, Antitumour imidazotetrazines. Part 12. Reactions of mitozolomide and its 3-alkyl congeners with oxygen, nitrogen, halogen, and carbon nucleophiles. *J. Chem. Soc., Perkin Trans. 1* 665 (1987).

58. J. W. Lown, R. Singh, Synthesis of 3(2-haloethyl)aryltriazenes and study of their reactions in aqueous solution. *Can. J. Chem.* **59**, 1347–1356 (1981).

59. D. Cousin, J. Zhang, M. G. Hummersone, C. S. Matthews, M. Frigerio, T. D. Bradshaw, M. F. G. Stevens, Antitumor imidazo[5,1-d]-1,2,3,5-tetrazines: Compounds modified at the

3-position overcome resistance in human glioblastoma cell lines. *MedChemComm* **7**, 2332–2343 (2016).

60. Y. F. Shealy, C. A. O'Dell, C. A. Krauth, 5-[3-(2-Chloroethyl)-1-triazenyl] imidazole-4-carboxamide and a possible mechanism of action of 5-[3, 3-bis(2-chloroethyl)-1-triazenyl] imidazole-4-carboxamide. *J. Pharm. Sci.* **64**, 177–180 (1975).

61. M. Koi, A. Umar, D. P. Chauhan, S. P. Cherian, J. M. Carethers, T. A. Kunkel, C. R. Boland, Human chromosome 3 corrects mismatch repair deficiency and microsatellite instability and reduces *N*-methyl-*N*'-nitro-*N*-nitrosoguanidine tolerance in colon tumor cells with homozygous hMLH1 mutation. *Cancer Res.* **54**, 4308–4312 (1994).

62. W. Sakai, E. M. Swisher, C. Jacquemont, K. V. Chandramohan, F. J. Couch, S. P. Langdon, K. Wurz, J. Higgins, E. Villegas, T. Taniguchi, Functional restoration of BRCA2 protein by secondary *BRCA2* mutations in *BRCA2*-mutated ovarian carcinoma. *Cancer Res.* **69**, 6381–6386 (2009).

63. C. McQuin, A. Goodman, V. Chernyshev, L. Kamentsky, B. A. Cimini, K. W. Karhohs, M. Doan, L. Ding, S. M. Rafelski, D. Thirstrup, W. Wiegraebe, S. Singh, T. Becker, J. C. Caicedo, A. E. Carpenter, CellProfiler 3.0: Next-generation image processing for biology. *PLOS Biol.* **16**, e2005970 (2018).

64. J. H. Wu, N. J. Jones, Assessment of DNA interstrand crosslinks using the modified alkaline comet assay. *Methods Mol. Biol.* **817**, 165–181 (2012).

65. Y. V. Surovtseva, V. Jairam, A. F. Salem, R. K. Sundaram, R. S. Bindra, S. B. Herzon, Characterization of cardiac glycoside natural products as potent inhibitors of DNA double-strand break repair by a whole-cell double immunofluorescence assay. *J. Am. Chem. Soc.* **138**, 3844–3855 (2016).

66. S. Oeck, N. M. Malewicz, S. Hurst, J. Rudner, V. Jendrossek, The Focinator—A new open-source tool for high-throughput foci evaluation of DNA damage. *Radiat. Oncol.* **10**, 163 (2015).

67. S. Oeck, N. M. Malewicz, S. Hurst, K. Al-Refae, A. Krysztofiak, V. Jendrossek, The Focinator v2-0—Graphical interface, four channels, colocalization analysis and cell phase identification. *Radiat. Res.* **188**, 114–120 (2017).

68. G. K. Chan, T. L. Kleinheinz, D. Peterson, J. G. Moffat, A simple high-content cell cycle assay reveals frequent discrepancies between cell number and ATP and MTS proliferation assays. *PLOS ONE* **8**, e63583 (2013).